Chapter 3
Biomedical Integrated Instrumentation

Abstract This Chapter is focused on the development of an integrated instrumentation to work with three electrodes amperometric Biosensor. First of all, it is introduced the conception of three electrodes configuration and how it works. Moreover, some typical electrochemical techniques like Voltammetry, EIS and amperometry, are introduced to the reader. The instrumentation electronics is based on a potentiostat architecture, which is explained in detail and experimentally validated. The obtained results with the full-custom approach are compared with the ones obtained using a commercial potentiostat. In that way, the correct operation of the designed circuits is fully validated. Furthermore, this chapter explains the conception of a Lock-In amplifier circuit used to detect the real and imaginary components of the complex impedance measured from the Biosensor. This circuit is theoretically explained and some simulated results are shown. Finally, the conception of Biotelemetry or how to transmit information from the subcutaneous device to the external reader is introduced. Then, the implemented protocol in this work is detailed. In summary, this chapter presents the developed BioChip IC that is able to drive the sensor, process the measured data and transmit the data to the external side through an inductive link.

Keywords Analog integrated circuits · Microelectronic implants · Bioimpedance · Amperometric sensors · Electrochemical impedance spectroscopy · Phase detection · Active filters · Biomedical telemetry

3.1 General Introduction to Biomedical Instrumentation

A biomedical instrumentation system comprises [1], basically, the modules presented in Fig. 3.1. Its general architecture is similar to other conventional instrumentation system [2, 3]. The main difference between the bioinstrumentation and the conventional ones is the sort of signals to be analyzed. In Biomedical Systems (BS), the signals come from activities related with the human body and they have to be measured in-vivo through the living tissue, or using microelectrodes to detect biological activities [4, 5] or in-vitro, outside the human body [6].

J. Colomer-Farrarons, P.L. Miribel-Català, *A CMOS Self-Powered Front-End Architecture for Subcutaneous Event-Detector Devices*, DOI 10.1007/978-94-007-0686-6_3,

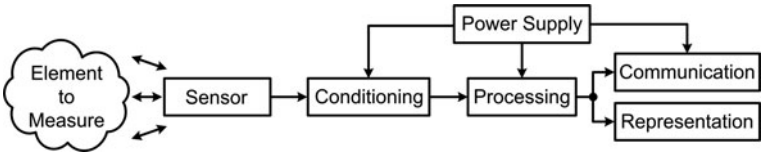

Fig. 3.1 General instrument architecture

The *Element to Measure or "Measurand"* [2, 3] is the value, property or physical quantity to be sensed and detected. In biomedical instrumentation this element could be a substance concentration, biopotential, pressure, impedance, etc. . .

The *Sensor* module is in charge to convert the energy generated by the *Measurand* to an electrical form [2, 4, 7, 8–10, 11]. This module is also known as transducer. There are several types of Biosensors, from the typical skin electrodes [5, 6, 12] used in electrocardiograms, till the miniaturized electrodes used to detect glucose, ADN . . ., but all of them have to be specifically designed to extract the minimum amount of energy to be minimally invasive with their surroundings.

The output of the sensor is sometimes not enough valid to be processed. Hereby, the *Signal Conditioning* module prepares the output to be treated and analyzed. It could amplify, filter and even digitalize the incoming signal in order to prepare it for the following step. Once the signal is conditioned, the *Signal Processing* module evaluates the data and takes the necessary actions. At this stage, the data is organized and it could be displayed in a monitor or in the same device, or the module could activate an alarm if a threshold value is exceeded. Moreover, the *Signal Processing* module may prepare the data to be transmitted to other locations like a PC or a remote host.

Finally, if a communication is required, the *Communication* module is in charge to do that. It transmits the data prepared by the processing unit to the receiver or receivers using the established protocols, like TCP/IP, series, parallel, etc. . . It can transmit the information using cables or providing a wireless link between the medical instrument and the receiving unit, known as a Biotelemetry. It is a really useful tool since it allows transmitting information about one patient, i.e. in a hospital room, to the monitoring center without using the lengthy and cumbersome cables and giving full autonomy to the patient.

The energy in Fig. 3.1 is provided by the *Power Supply* unit. It manages the main energy source, battery, power line, harvesting, and delivers the necessary voltage and current to each module. It has to be carefully designed in order to guarantee the best isolation between the energy source and the electronic modules and *Measurand*, i.e., the patient. For implanted subcutaneous devices, inductive powering is one of the most useful methods to power the internal circuitry. The architecture shown above is not unique. It could be adapted by eliminating, adding or replacing some modules. Sometimes, *Processing* and *Communication* are joined in a single module and an extra calibration unit is added [13] in portable equipment. Moreover, some control feedback is included to adjust automatically drifts due to temperature or sensors degradation.

If the developed instrument is for implantable applications, inside human body, some extra considerations have to be done. First of all, the size of the instrument is very important. Given the human body dimensions, instruments not higher than a few cm are mandatory. Moreover, the consumption of those devices have to be really small hence, low-voltage low-power integrated instruments are the solution.

A perfect isolation between the instrument and its biological environment is a must in order to avoid biocompatibility and thermal problems. A temperature variation between one or two Celsius degree could produce injuries in the body and sensing problems.

3.2 Electrochemical Biosensors

A Biosensor is a type of sensor able to convert the biochemical interactions produced in a biological material into electrical or optical signals [14] allowing the detection of substances like enzymes [15, 16], antibodies [17, 18], proteins [19], etc...

Basically, it is formed by two parts: the Bioreceptor or biological detection element, which recognizes the element to be studied (enzymes, antibodies, etc...) and the Transducer that detects the biological reaction in the Bioreceptor and generates a proportional electrical signal. Depending on the type of Transducer the response of the Biosensor could be Potentiometric [19, 20], Amperometric [16, 21], Conductometric [22, 23], etc...

The electronics developed here are focused on working with low-frequency Amperometric [24, 25] Biosensor. An Amperometric sensor generates a current when a potential is applied on the electrochemical cell, which is proportional to the electrochemical reactions produced in the Bioreceptor. On the other hand, capacitive Biosensor produces a variation on its capacitance when a reaction takes place in the Bioreceptor hence, an impedance variation is produced in the electrode-solution interface when an AC signal is applied on the cell [14]. This means that an amperometric sensors delivers the electrochemical information by modulating the current through it, whereas, on Capacitive sensors the information is done by modification of the sensor impedance.

In general, amperometric and capacitive sensors are based on the use of 2 or 3 electrodes, Fig. 3.2. The most used topology is the three electrodes cell because it allows a better control of the applied potential to the cell. So, the developed instrumentation is for 3-electrodes sensors.

The function of each electrode is described below:

- *Counter* or *Auxiliar Electrode* (C/A): it supplies the necessary current required for the reaction at the W electrode.
- *Reference Electrode* (R): it is used to measure the potential between the *Reference* and *Working* electrodes in order to control the biochemical reaction.
- *Working Electrode* (W): it is covered with a sensitive film that serves as a surface where the reaction takes place.

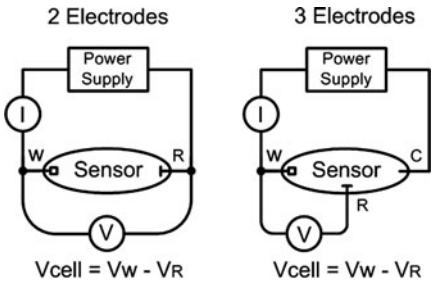

Fig. 3.2 Two and three electrodes sensor configuration

Mainly, the three electrodes sensor works as follows: a current flow (I, Fig. 3.2) is generated between C and W electrodes when a potential is applied between them (Power Supply). However, the electrochemical reaction starts on the W electrode when a well-known potential (V) is established between the *Reference* and *Working* electrodes.

A specific electronic circuit, known as potentiostat, is used to control the voltage between the R and W and to inject the current through the *Counter* electrode. Furthermore, it also measures the current flowing in the *Working* electrode. There are several options to develop this kind of circuits, from full analog solutions to mixed implementations. In that work, the integrated potentiostat is based on an analog development using operational amplifiers.

3.2.1 Three Electrodes Sensor Model

An electrochemical reaction could be described as a network of resistances, capacitances or impedances and active elements [26, 27]. These electrical equivalent circuits are important to understand the behavior and the working principle of the sensors. Moreover, these models are also used to design and test the sensor's electronics.

The representation of the interface model can be very complex [27]. The simplest case uses an equivalent circuit called Randles circuit [28]. It is presented in Fig. 3.3 and it is composed by the double-layer capacitor (C_{ref}), the polarization resistor (R_{ref}), which is also described as a charge transfer resistor, and the solution resistor (R_{AUX}).

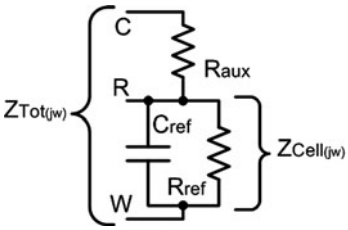

Fig. 3.3 Electrochemical Randles sensor model

These parameters are time-dependent and they have to be roughly known with an estimation that extends a couple of decades [29]. Then, the values of these parameters are used to guarantee stable operation of the implemented electronic circuit.

An important element is the presence of the capacitor, which is used to model the interface between the electrode and their surrounding electrolyte. This capacitive Biosensor is based on the theory of the electrical double-layer [30]. An electrode immersed in an electrolyte solution can be generally described as a capacitor in its ability to store charge. The double layer capacitor is formed as ions from a solution absorbed on the electrode surfaces.

The total impedance of the equivalent sensor model presented in Fig. 3.3 is defined by (3.1)

$$Z_{Tot}\,(jw) = \frac{V_{WC}(jw)}{I_C(jw)} = R_{aux} + \frac{R_{ref}}{1 + R_{ref}C_{ref}(jw)} \tag{3.1}$$

whereas the sensor Cell Impedance, where the reaction takes place, is defined by (3.2)

$$Z_{Cell}\,(jw) = Z_{W-R}\,(jw) = \frac{V_{WR}(jw)}{I_W(jw)} = \frac{R_{ref}}{1 + R_{ref}C_{ref}(jw)} \tag{3.2}$$

From (3.2), the real and imaginary parts of the impedance are derived.

$$Z_{Cell}\,(jw) = Z_{W-R}\,(jw) = \underbrace{\frac{R_{ref}}{1 + R_{ref}^2 C_{ref}^2 w^2}}_{Z_{REAL}} - \underbrace{\frac{R_{ref}^2 C_{ref} jw}{1 + R_{ref}^2 C_{ref}^2 w^2}}_{Z_{IMAG}} \tag{3.3}$$

Using this mathematical approach, it is possible to identify each electrical component of the model and relate each value with the corresponding electrochemical effect in the reaction. If there is some reaction in the sensor, automatically the corresponding electrical parameter will be modified and the impedance will change. Moreover, complex models can be developed just connecting, in series or parallel, more electrical components [31] to accurately describe the sensor behavior and some effects like Warburg resistance [32].

From Eqs. (3.1) and (3.3) can be deduced that applying an AC voltage signal (frequency dependent) to the sensor, it is possible to extract the real and imaginary part of the whole impedance.

On the other side, when a DC signal is applied just the real part is extracted. This means that it is possible to deduce all the impedance components combining DC and AC analysis techniques. These techniques, as well as their representations, are explained in the next section.

3.2.2 Cyclic Voltammetry, Amperometry, Impedance Analysis (EIS) and Their Representations

Several analysis techniques can be carried out with Biosensors in order to extract information about the analyzed substance. Some of the most used techniques are cyclic voltammetry [33, 34], amperometry [35], potentiometric analysis and EIS (Electrochemical Impedance Spectroscopy) [36]. Each technique will be applied in function of the type of sensor and substance to be analyzed.

The instrumentation developed here is designed to work with cyclic voltammetry and amperometric analysis and also prepared to perform low-frequencies *EIS* analysis.

The *Cyclic Voltammetry (CV)* method is widely used to study the products of electrochemical Reduction – Oxidation (Redox pair) reactions in the electrode/solution interface. It applies a triangular potential (Fig. 3.4a) between the R – W electrodes while the current through the *Working* is measured.

Then, this current is represented in function of the applied voltage (Fig. 3.4b). In that analysis, the max and min voltages, as well as the slope of the triangular wave, have influences in the reaction [37].

At the beginning of the analysis (point a, Fig. 3.4b) the generated current is small. Then, the current increases because the voltage approximates to the reduction potential (ab) and the electrons are forced to move from the electrode toward the analyzed substance. The maximum transfer is achieved at the Reduction potential (b).

Once the voltage overcomes the Reduction potential (V_{red}) the current generated decreases till point (c). Then, the current starts to decrease when the voltage

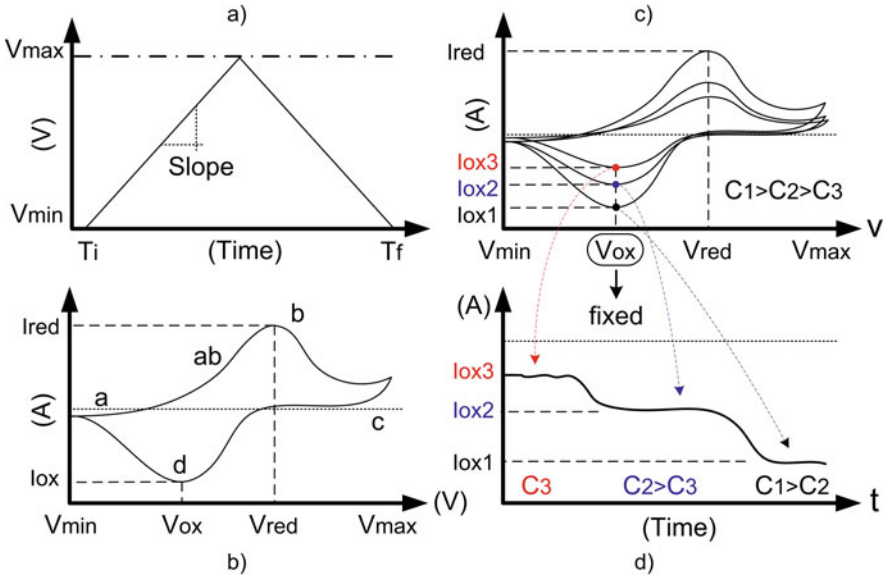

Fig. 3.4 (**a**) Cyclic voltammetry (CV) potential waveform; initial (T_i) and final (T_f) time and maximum (V_{max}) and minimum (V_{min}) voltage, (**b**) CV plot or voltammogram; oxidation and reduction potentials (V_{ox}, V_{red}) and currents (I_{ox}, I_{red}), (**c**) Several CV carried out with the same solution at different concentrations **c** and (**d**) amperogram; fixing a DC potential measure the current

is reversed because the electrons are forced to move from the substance to the electrode, defining the reversible Redox reaction. The minimum current is achieved when the applied voltage is the oxidation potential (d).

The current generated is proportional to the concentration of the analyzed substance and the size of the electrodes [38]. So, if the same analysis with the same type of sensors is carried out in the same substance at two different concentrations, the generated reduction and oxidation currents are different as it is showed in Fig. 3.4c.

At that point, the conception of the *Amperometric* analysis could be introduced. A DC amperometric configuration consists in applying a constant voltage at the $R - W$ electrodes and measuring the current at the *Working* electrode.

Generally, the applied DC voltage is a potential where the electrochemical reaction is maximized. Then, the substance concentration could be continuously monitored and represented in an amperogram. Fig. 3.4d presents the idea of the amperogram using the Oxidation voltage as a fixed potential.

Electrochemical Impedance Spectroscopy (EIS) technique consists in applying an AC voltage to the $R - W$ electrodes and measuring the resulting AC current at the *Working* electrode. Then, it is possible to represent the impedance, or capacitance, variations of the analyzed substance dividing the AC voltage by the current as it is described in Eqs. (3.2) and (3.3).

The typical representation of the EIS is the Nyquist diagram, where the imaginary part of the impedance is plotted against the real one for several frequencies (from low to high frequencies) [36].

Figure 3.5 presents a Nyquist plot for the ideal model introduced in Fig. 3.3. If there is a modification in the concentration of the target substance, the total

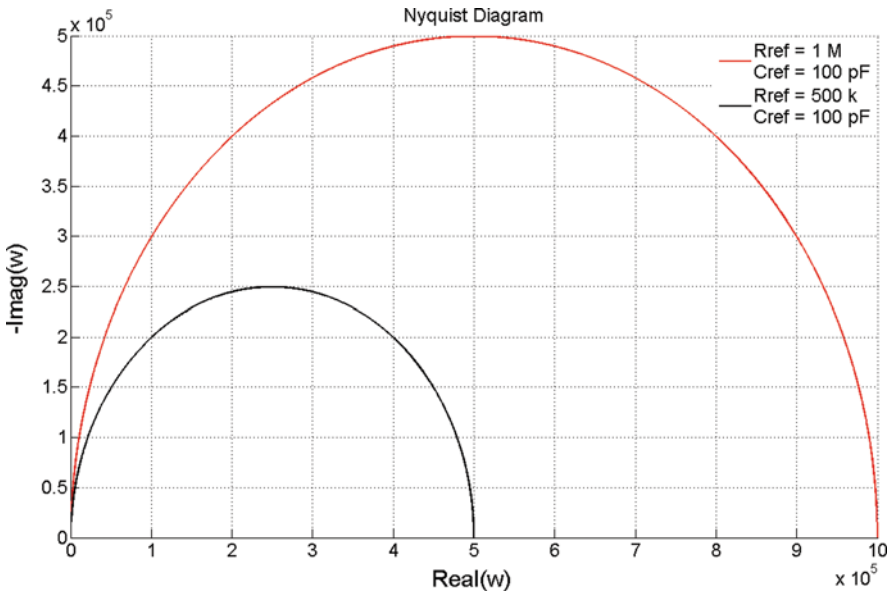

Fig. 3.5 Nyquist plot derived from computer generated data using Eq. (3.3)

impedance of the sensor is also modified as well as the Nyquist plot (i.e. in capacitive sensors the impedance is modified in function of the sensor capacitance, which varies in accordance with the amount of substance detected). Moreover, there are other types of EIS representation like bode plots, where the real and imaginary values are plotted in function of the frequency [24].

Similar to the previous concept of DC amperometric analysis there is the AC amperometry. It consists in using an AC signal at one defined frequency, where the sensor is more sensitive to impedance variations. In that way, the real and imaginary part of the impedance could be continuously controlled at the defined frequency by simply using a specific electronic circuit.

3.3 Potentiostat (Sensor Instrumentation)

The Potentiostat Amplifier (PA) [39, 40, 41] is the name of the electronic instrumentation in charge to control the three Biosensor electrodes. Basically, the PA is formed by two main blocks: Control (CM) and Transimpedance Modules (TIA), Fig. 3.6. The CM keeps the difference voltage between the *Reference* (R) and *Working* (W) electrodes constant by following a well-known input signal (V_{in}). On the other hand, the Detection Module (TIA) measures the current flowing through the W and it also provides a virtual ground to the *Working* electrode.

In the adopted implemented architecture, the Control Module is based on a comparator configuration and a buffer stage, whereas the Detection Module is formed by a Current – to – Voltage converter (TIA). The selected topology is depicted in

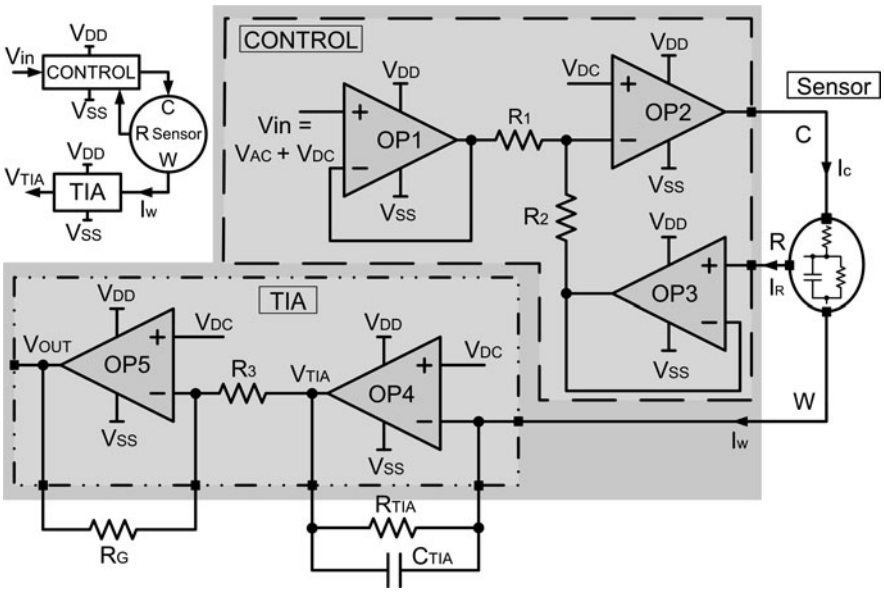

Fig. 3.6 Potentiostat architecture, generic *block diagram* (*white*) and implemented structure (*grey*)

Table 3.1 Potentiostat expected features

Symbol	Parameter	Min	Max	Units
P_{SUPPLY}	Power consumption		< 200 μ	W
V_{SUPPLY}	Voltage supply	±0.6 (1.2)	±1.2 (2.5)	V
V_{in}	Input voltage to apply at V_W-V_R	±10 m	±1	V
Freq.	Frequency at V_W-V_R	DC	10 k	Hz
I_{DET}	Current conversion (I_W)	1 n	100 μ	A

Fig. 3.6 and it is formed by five amplifiers, OP_1 to OP_5, and three resistors, R_1 to R_3. R_{TIA} and R_G are off-chip resistors [42, 43].

The designed potentiostat is focused on Low-Voltage Low-Power applications, like integrated in-vivo monitoring or detection [44], and it is designed to work with low-frequency integrated electrochemical Biosensors [29, 45, 46]. Moreover, the selected topology presents a good trade-off in terms of design simplicity and performance reliability. Table 3.1 summarizes the desired features for the PA.

3.3.1 Control Module (CM)

The Control Module is the specific part of the potentiostat designed to manage the voltage applied to the sensor. This circuitry is in charge to apply and to control the input voltage (V_{IN}) between the *Working* (W) and *Reference* (R) electrodes, such that, $V_{in} = V_W – V_R$ where, V_R is the voltage at the *Reference* electrode and V_W at the *Working* electrode. The adopted CM is based on three operational amplifiers, OP1, 2, and 3, Fig. 3.6.

OP3 monitors continuously the potential (V_R) at the *Reference* electrode, in that way, it is possible to control the voltage drop between W and R. Furthermore, OP 3 is used to ensure a minimal current flow through the R electrode (ideally zero) so, it is possible to assume that:

$$\left.\begin{array}{c} I_C = I_R + I_W \\ I_R \cong 0 \end{array}\right\} \rightarrow I_C = I_W \tag{3.4}$$

where I_C is the current flowing from the Counter or *Auxiliary* electrode, I_R the current in the *Reference* electrode and I_W the current flowing through the *Working* electrode. The Reference voltage (V_R) is then compared with the input voltage (V_{in}) by OP2 defining the voltage applied at the reference electrode:

$$\left.\begin{array}{c} \dfrac{V_{in} - V_{DC}}{R_1} = \dfrac{V_{DC} - V_R}{R_2} \\ R_1 = R_2 \end{array}\right\} \rightarrow \left.\begin{array}{c} V_{in} = -V_R + 2V_{DC} \\ V_{DC} = 0 \end{array}\right\} \rightarrow V_{in} = -V_R \tag{3.5}$$

Since $V_W = 0$ thanks to a virtual ground connection (Section 3.3.2), the cell voltage V_{Cell} is given by,

$$\left.\begin{array}{c} V_{Cell} = V_W - V_R \\ V_W \cong 0 \end{array}\right\} V_{Cell} = -V_R \tag{3.6}$$

Using this CM architecture it is possible to easily control the cell voltage and, hence, to control the electrochemical reaction. Finally, OP1 isolates the input voltage from the rest of the circuit. Regarding resistors R1 and R2, it is important to take into account their values. Small values increase the consumption of the potentiostat. Otherwise, the use of high resistance values could produce noise [47] and operational problems. Moreover, a careful layout between them is a must in order to avoid mismatch problems and to reduce the final size of the integrated resistors.

From the previous explanation, it is deduced that amplifiers OP1, OP2 and OP3 have to be designed taking into account some considerations. OP2 requires a high output current capability to drive properly the *Auxiliar* electrode, whereas OP3 requires a low input bias current in order to guarantee a minimum current flowing in the *Reference* electrode. The maximum operation frequency is also another important aspect to evaluate. If the desirable working frequency of the potentiostat is 10 kHz (Table 3.1) this implies a unity frequency of, at least, 1 MHz for each amplifier [47–49].

Figure 3.7 shows the selected architecture of the amplifier designed to accomplish all the design constrains introduced on Table 3.2. It is composed by a differential PMOS input stage with a folded cascode current multiplier stage followed by an AB output buffer. This topology presents a high output current and slew rate capability for OP2 and low input bias current around 600 pA, enough for OP3.

A differential PMOS input pair is used to assure a good response for low voltages closed to 0 V [50], whereas a folded cascode current multiplier is implemented to achieve enough gain and stability. Finally, a class AB output is selected as output stage for its high current output capability, high slew rate and reduced power consumption.

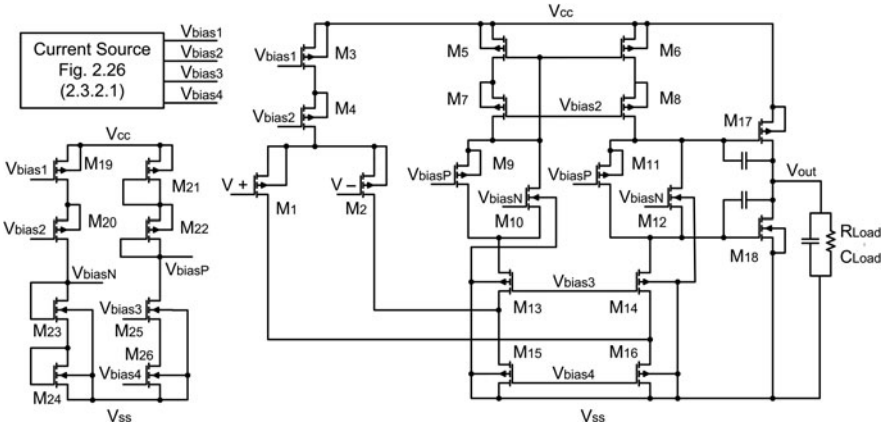

Fig. 3.7 Schematic of the class AB operational amplifier for OP1, OP2 and OP3

Table 3.2 Control module operational amplifiers design constrains

Amplifier	Constrains
OP1; OP2; Op3	↑ Unity frequency (f_u) around 1 MHz
OP1; OP2; Op3	↓ Minimum input voltages
OP2	↑ Output current
OP3	↓ Input bias current

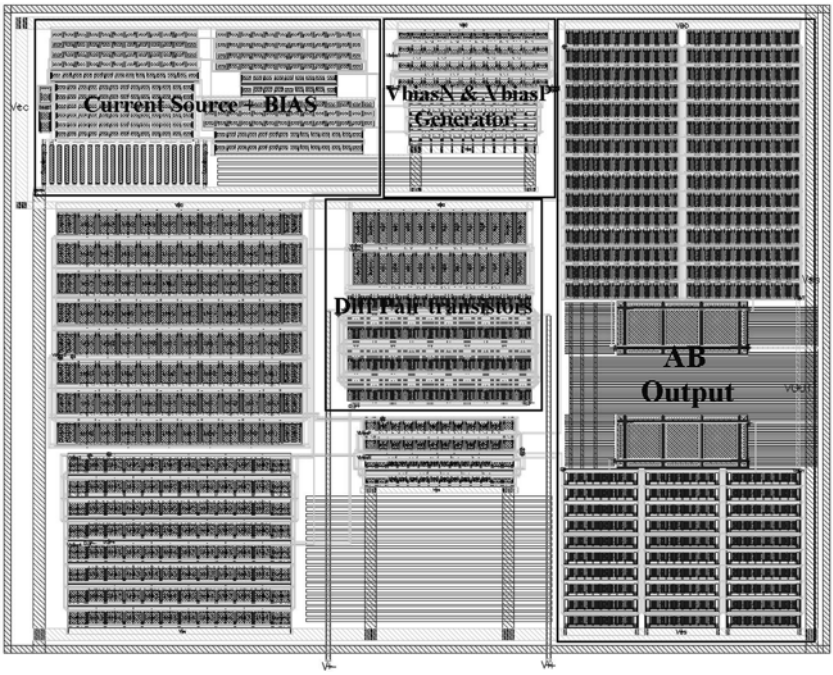

Fig. 3.8 2.5 V AB operational amplifier layout (445 μm × 656 μm)

Two different layouts have been designed. The first one focuses on working with 2.5 V (±1.2 V) supply voltage and optimizing the matching using symmetrically structures, Fig. 3.8. Its main drawback is the huge size of its layout around 445 μm × 565 μm. The second layout prepared to work with a supply voltage up to 1.2 V (±0.6 V) is also implemented. Its layout structure is similar to those shown in Fig. 2.25 involving a total size of 180 μm × 50 μm, which is ideal for small, portable and low-power System on Chip. Table 3.3 summarizes the experimental electrical feature for each amplifier, 2.5 and 1.2 V voltage supply.

At this stage let us analyze the stability of the Control Module. It is important to assure a perfect stability for all load conditions range (sensors) that the potentiostat could work. In that way, problems regarding wrong measurements, wrong

Table 3.3 Class AB amplifier experimental features ($R_{Load} = 1\ M\Omega$, $C_{Load} = 20\ pF$)

Symbol	Parameter	Value		Units
V_{CC}	Power voltage	1.2 (±0.6)	2.5 (±1.2)	V
V_{Offset}	Offset voltage	–15.84	–7.92	μV
F_U	Unity frequency	448.88	632.17	kHz
Ph	Phase margin	59.32	61.19	°
G_{DC}	DC Gain	105.64	115.13	dB
V_{noise}	Noise	16.41	14.89	μV
V_{noise}	Noise	–95.7	–96.54	Db
I_{CC}	Current consumption	57.462	74.696	nA
P_{CC}	Power consumption	68.655	186.74	μW
SR @ 10 kHz	Slew rate	0.1927	0.2608	V/μs
SR @ 10 kHz	Slew rate	0.1783	0.2971	V/μs
Size	W × L	180 × 50	445 × 565	μm × μm

sensor polarization or even extra heating dissipation in the AB operational or in the potentiostat could be solved.

Basically, the stability involves resistances, R_1 – R_2 operational OP1, 2 and 3, and the *Auxiliar* and *Reference* electrodes. It is also assumed a perfect grounded connection of the *Working* electrode through the Transimpedance Amplifier OP4 (Section 3.3.2). Hence, there is no influence coming from this part of the circuit to the whole stability. Moreover, voltage follower amplifiers OP1 and OP3 can be treated as a short circuit connection in order to reduce the complexity of the analysis.

3.3.2 Detection Module (I-to-V Conversion)

The Detection Module, as the name indicates, is in charge to detect the current flowing in the *Working* electrode, which is the current generated by the electrochemical reaction. The implemented solution is a Current – to – Voltage converter based on a Transimpedance Amplifier (TIA).

Basically, the Transimpedance Amplifier has two main functions: the first one, as it is commented above, consists on measuring the current in the W electrode; whereas the second function consists in providing a virtual ground to the *Working* electrode in order to guarantee Eq. (3.6) and hence, the correct operation of the potentiostat.

The Detection Module based on a TIA is formed by OP4 and the programmable feedback resistance R_{TIA} as it is depicted in Fig. 3.6. The current – to – voltage conversion is done such that,

$$\left.\begin{aligned} V_{TIA} &= -I_W R_{TIA} \\ V_{OUT} &= -V_{TIA}\frac{R_G}{R_3} \end{aligned}\right\} \rightarrow V_{OUT} = I_W R_{TIA}\frac{R_G}{R_3} \tag{3.7}$$

where I_W is the current through the *Working* electrode. Then, combining Eqs. (3.2) and (3.7) and taking into account the virtual ground connection in the W electrode, it can be demonstrated that the Cell Impedance (Z_{CELL}) is described by:

$$Z_{Cell}(jw) = Z_{W-R}(jw) = \frac{V_W - V_R}{I_W}(jw) = \frac{V_R}{V_{OUT}}(jw)\frac{R_{TIA}R_G}{R_3} \tag{3.8}$$

In that way, combining the Control Module and the TIA, it is possible to detect continuously the current, Eq. (3.7), and the impedance Eq. (3.8) of the biochemical interaction. Voltammograms and DC amperograms could be represented directly by using the proportional voltage V_{OUT}, whereas for impedance detection an extra circuit is needed to find out the real and imaginary part (Section 3.4).

At the input of the TIA amplifier a high input resistance is necessary in order to generate properly the virtual ground and the current conversion. If the resistance is not high enough two drawbacks could appear: first, I-to-V conversion errors due to high input bias currents and second, noise problems at the *Working* electrode modifying the virtual ground connection. To avoid those problems, JFET transistors are the perfect choice to be used in the input pair thanks to its high gate input resistance ($\approx 10\ G\Omega$) [51, 52]. Otherwise, extra specific input stages are necessary to increase the input resistance if only MOSFET transistors are available.

The final TIA architecture is presented in Fig. 3.9. It is based exclusively on MOSFET transistors. It is formed by a modified input stage to generate a high input resistance ($\approx G\Omega$) and a folded cascode as a second stage. Its input stage is composed by a PMOS differential transconductance pair (M1 M2) with small width transistors to increase the input resistance [53]. Then, an extra differential PMOS

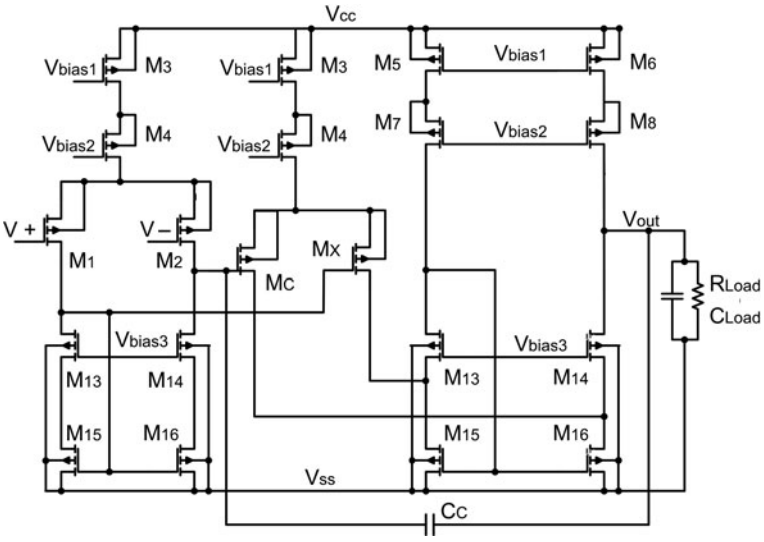

Fig. 3.9 Schematic architecture of the TIA amplifier

pair (MX MC) is added to increase both, the input resistance and also the gain of the whole input stage.

Finally, a folded cascode is implemented as a second and output stage. This circuit increases the input resistance as well as the total gain. Moreover, it isolates the input and output stages while increasing the total bandwidth [53]. An extra capacitor C_C (5 pF) between the input and the output assures the stability for the whole frequency range.

Since the output stage is an ordinary folded cascode, it is not possible to drive enough current at the output, so it must be followed by an extra Gain amplifier (OP5), which is based on the class AB presented in Fig. 3.7.

Following the same idea introduced in the Control Module, two different layouts have been designed. The first one focuses on working with 2.5 V and on optimizing the matching using symmetrically structures, similar to Fig. 3.8. Its main drawback also concerns its size of 280 μm $\times$ 390 μm.

The second layout prepared to work with a supply voltage up to 1.2 V ($\pm$0.6 V) is also made. Its layout structure is similar to the one shown in Fig. 2.25 a total area of 180 μm $\times$ 50 μm ideal for small, portable and low power Systems on Chips. Table 3.4 summarizes the experimental electrical feature for each TIA.

A feedback capacitor C_{TIA}, Fig. 3.6, could be added in parallel with R_{TIA} in order to control the frequency response of the Transimpedance Amplifier and to define a frequency filter [47, 54]. The cut-off frequency could be easily calculated using Eq. (3.9) for a simple filter response.

$$f_{cut-off}^{TIA} = \frac{1}{(2\pi R_{TIA} C_{TIA})} \tag{3.9}$$

The previous filter approach does not take into account the impedance of the Sensor Cell. Hence, other type of filter responses could be adapted for more accurate frequency restrictions. A 2nd order Butterworth [55] response is obtained following Eq. (3.10):

$$\frac{1}{(2\pi R_{TIA} C_{TIA})} = \sqrt{\frac{GBP}{(4\pi R_{TIA} Z_{Cell})}} \tag{3.10}$$

Table 3.4 TIA experimental electrical features $R_{Load} = 1$ MΩ, $C_{Load} = 20$ pF

Symbol	Parameter	Value		Units
V_{CC}	Power voltage	1.2 ($\pm$0.6)	2.5 ($\pm$1.2)	V
V_{Offset}	Offset voltage	23.1	14.36	μV
F_U	Unity frequency	398.68	570.17	kHz
Ph	Phase margin	54.23	63.9	°
G_{DC}	DC Gain	70.57	85	dB
R_{IN}	Input resistance	1.02	1.85	GΩ
I_{CC}	Current consumption	30.25	51	nA
P_{CC}	Power consumption	35.41	118.64	μW
Size	W $\times$ L	180 $\times$ 50	280 $\times$ 390	μm $\times$ μm

where GPW is the gain bandwidth product of the TIA and the Z_{Cell} is the impedance between *Working* and *Reference* electrodes. In that implementation, it is important to know an approximate value of the Z_{Cell} range to design properly the cut-off frequency, Eq. (3.11).

$$f_{cut-off}^{TIA-But} = \sqrt{\frac{GBP}{(4\pi R_{TIA} Z_{Cell})}} \tag{3.11}$$

3.3.3 Results

Two potentiostats are designed in a commercial 0.13 μm technology (Appendix B) from ST Microelectronics. One of them is focused on low voltage operation up to ±0.6 V and low area consumption. The second one, as it is commented previously, is focused on working with a voltage up to ±1.2 V and on improving the layout matching. Figure 3.10 depicts the BIO-Chip with the two potentiostats as well as other circuits.

Several tests have been carried out in order to validate the Control and Detection modules of the potentiostat. First of all, the linearity and the PSRR of the potentiostat have been studied using some Randles models.

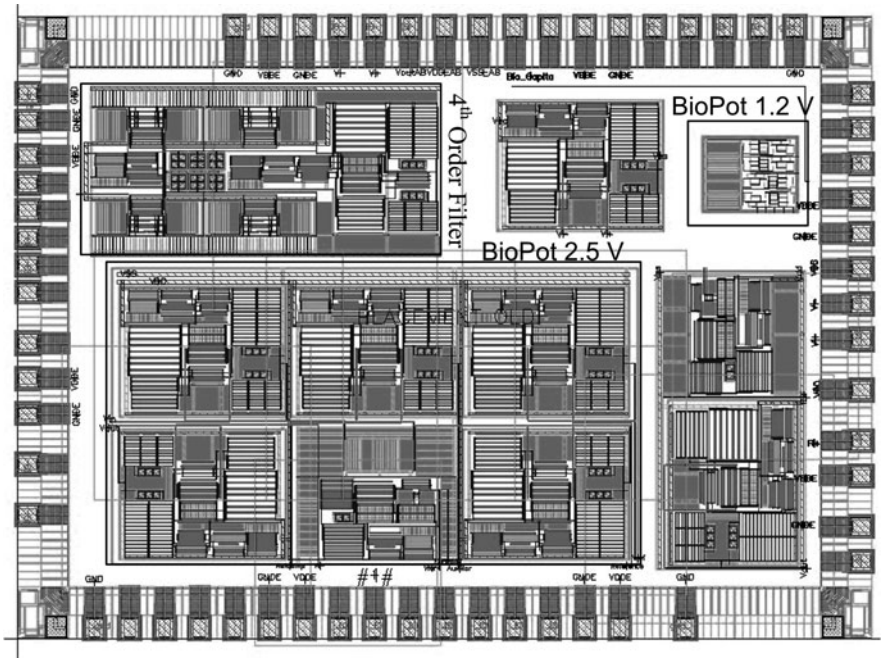

Fig. 3.10 Layout image of the IC "bio-chip" with the two designed potentiostats and the OTA filter

Then, the performances of the potentiostat are studied using several concentrations of potassium ferrocyanide, $K_4[Fe(CN)]_6$ [56] and a real sensor. Cyclic voltammograms and amperometric analysis are carried out and the results are compared with the ones obtained using a commercial instrument from CH Instruments [57].

The BVT Technologies AC1.W1.R1 [58] sensor is the selected option to proceed with the measurements. It is a ceramic based sensor formed by a gold working and auxiliary electrodes and a silver/silver chloride reference electrode. Furthermore, a bio-chemically active substance could be immobilized on the *working* electrode to create a Biosensor. That sensor is mainly focused on the measurements of glucose, ferricyanide, enzyme activity and basic electrochemical and bio-electrochemical techniques.

The test setup is composed by a LabVIEW [56] based software and a full-custom PCB for the IC socket, sensor and other connections. Figure 3.11 shows the PCB with the 68-pins BIO-Chip, the AC1.W1.R1 sensor and a capture of the LabVIEW main window; on it, a voltammogram and an amperometric analysis

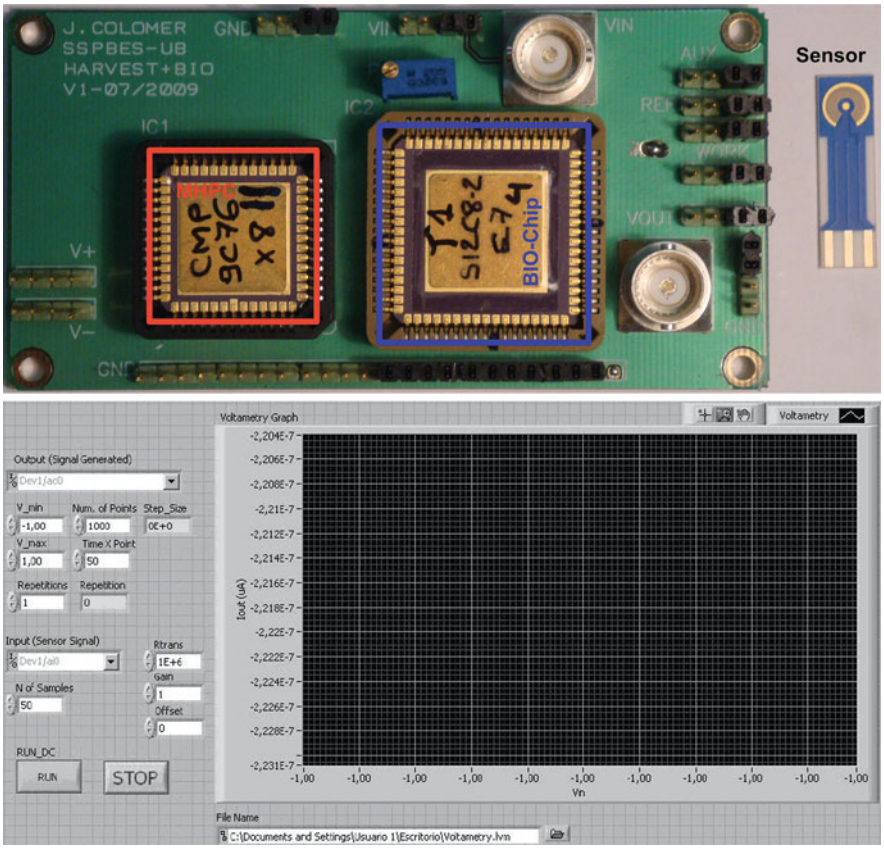

Fig. 3.11 PCB bio-chip test board with sensor connections and AC1.W1.R1 test sensor (*top*) and lab-view acquisition program main window (*bottom*) [55]

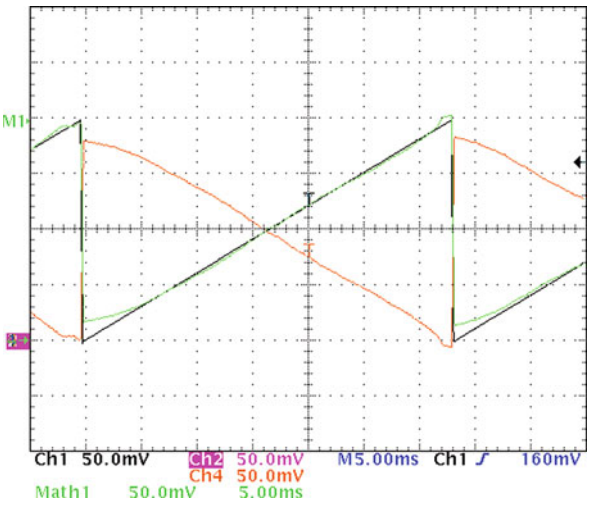

Fig. 3.12 Linear range of the 1.2 V potentiostat for an input ramp of 100 mV

could be realized (not at the same time). The results are displayed on the screen and stored in a plain file for post processing.

In order to represent the sensor cell, a Randles circuit formed by the double-layer capacitor ($C_{ref} = 100$ pF), in parallel with a polarization resistor ($R_{ref} = 100$ kΩ), which is also described as a charge transfer resistor, and the solution resistor ($R_{aux} = 50$ kΩ), has been used, Fig. 3.3.

The linearity of the potentiostat amplifier has been experimentally validated. The DC linear range for the 1.2 V (±0.6 V) potentiostat is ±0.54 V, whereas for the 2.5 V (±1.2 V) potentiostat is ±1.12 V with a deviation of less than 1% for both of them. Taking into account that small DC voltages could be applied for in vivo applications, the designed potentiostats have a correct range. Figure 3.12 depicts the cell voltage of the 1.2 V potentiostat for an input ramp up to 100 mV.

Experimental transient tests have been also carried out to analyze the AC performances and how the V_{Cell} follows an AC V_{in} signal. Figurer 3.13 shows the Working, the input and the TIA output voltages obtained with the 1.2 V potentiostat.

The Randles model uses a $R_{aux} = 3.9$ MΩ, $R_{ref} = 1$ MΩ and $C_{ref} = 100$ pF. The transimpedance resistance (R_{TIA}) is fixed at 1 MΩ. A sinus input signal is introduced with a DC component of 50 mV and an AC component of 100 mV_{PP} and a frequency of 1 kHz. The Total Harmonic Distortion (THD) is around 2%.

The frequency response of both potentiostats has also been studied. A fixed Randle model with $R_{aux} = 3.9$ MΩ, $R_{ref} = 1$ MΩ and $C_{ref} = 100$ pF allows defining a cut-off frequency (F_{-3db}) around 1,500 Hz. The ideal frequency response of the Cell Impedance is represented in Fig. 3.14.

Then, the experimental Z_{Cell} is obtained using Eq. (3.8) with $R_{TIA} = R_G = R_3 = 1$ MΩ. Both potentiostats have a maximum working frequency lower than 10 kHz, 2,200 Hz for 1.2 V potentiostat and 8,700 Hz for 2.5 V potentiostat. The 1.2 V potentiostat experimental responses could be compared with the theoretical ones in Fig. 3.14. There, it could be observed how the response of the potentiostat saturates in its maximum working frequency.

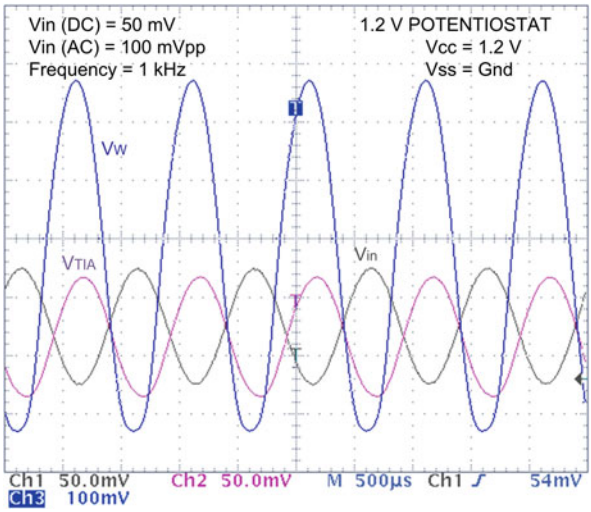

Fig. 3.13 1.2 V potentiostat AC response. V_W is the voltage at the working electrode. V_{in} is the input voltage and V_{TIA} is the voltage at the output of the transimpedance amplifier. A Randles model formed by $R_{aux} = 3.9\ M\Omega$, $R_{ref} = 1\ M\Omega$ and $C_{ref} = 100\ pF$ and a transimpedance resistance of 1 MΩ are used

Finally, both potentiostats have been calibrated before using them with real sensors. The calibration is done using several values of R_{ref} (470 kΩ, 1.2 MΩ, 1.5 MΩ, 5.6 MΩ) and applying a DC sweep between *Working* and *Reference* electrodes. Moreover, the R_{aux} resistance of the Randles model is replaced by a short

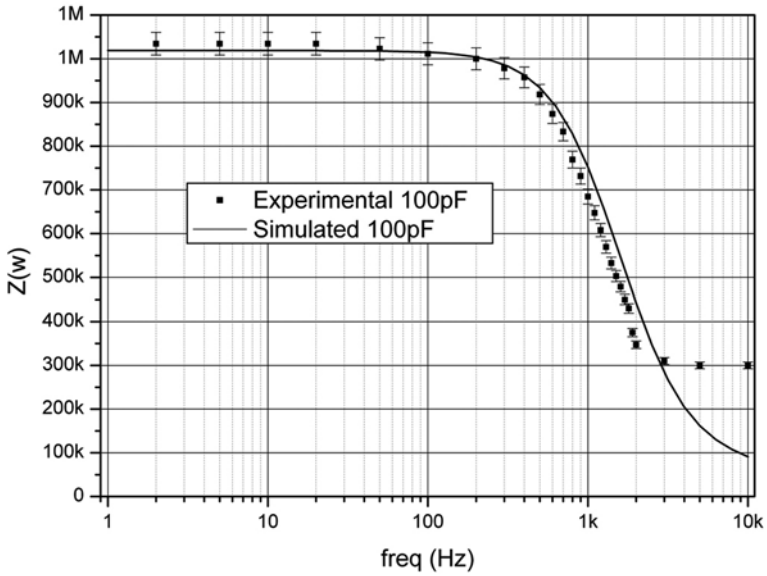

Fig. 3.14 1.2 V potentiostat frequency response

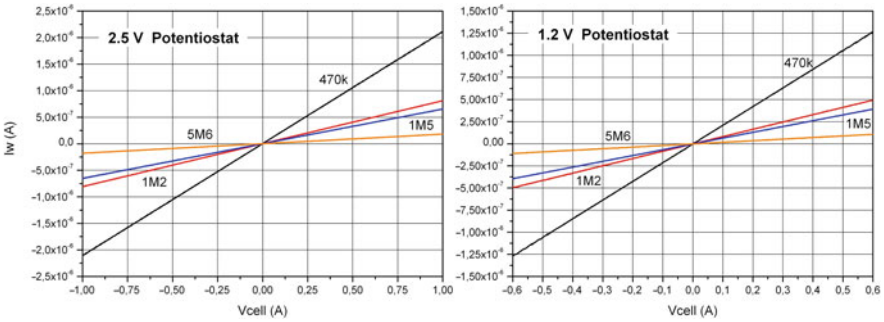

Fig. 3.15 Calibration curves for 1.2 and 2.5 V potentiostats for different R_{ref} values

circuit between *Counter* and *Reference* electrodes and the transimpedance (R_{TIA}) resistance is fixed at 1 MΩ in both cases.

The procedure is simple: a DC sweep is performed for each calibration resistance while reading the output voltage of the TIA. Then, the current ($I_W = V_{Cell}/R_{ref} = V_{TIA}/R_{TIA}$) is represented in function of the applied DC voltage (V_{Cell}), Fig. 3.15. The waveforms show that both potentiostats detect the correct current value for all voltages so, they are calibrated.

The last step consists in performing two electrochemical analysis, cyclic voltammetry and amperometric analysis, using five concentrations of $K_4[Fe(CN)]_6$ (1, 2, 3, 4 and 5 mM) in order to validate the designed integrated potentiostats. The results are compared with the ones obtained with the commercial instrument CHI 1232A from CH Instruments [57] (Appendix C shows some specifications).

The AC1.W1.R1 [58] sensor is connected to the potentiostats and a Cyclic Voltammetry (CV) from –1 to 1 V at 0.05 V/s is carried out with the 2.5 V potentiostat and the CH 1232A for all concentrations. A CV from –0.6 to 0.6 V at 0.05 V/s is done for the 1.2 V potentiostat. The results of each voltammetry are depicted in Fig. 3.16.

The shape of the electrochemical reaction is almost equal in all three potentiostats. The reduction and oxidation potentials are located around the same voltages of 0.170 V and 0.240 V for all potentiostats as can be observed in charts (d), (e), (f), (g) and (h).

The main difference lies in the current peak amplitude of the oxidation and reduction points. A 2.5 V integrated potentiostat presents maximum difference of 8 μA with respect to the commercial one. On the other hand, the 1.2 V potentiostat presents a higher difference around 12 μA; this could be caused by its lower input impedance than the 2.5 V potentiostat in the Transimpedance amplifier.

However, part of these differences is due to reproducibility errors of the electrochemical measure; it is not possible to obtain the same exact result every time it is performed the same experiment. The obtained CV waveforms are similar to those that can be found in the literature like [33, 35, 59–61].

The last electrochemical analysis consists on performing an amperometric analysis of several concentrations of $K_4[Fe(CN)]_6$ for the 2.5 and 1.2 V integrated potentiostats and then compare the results with those obtained with the commercial instrument.

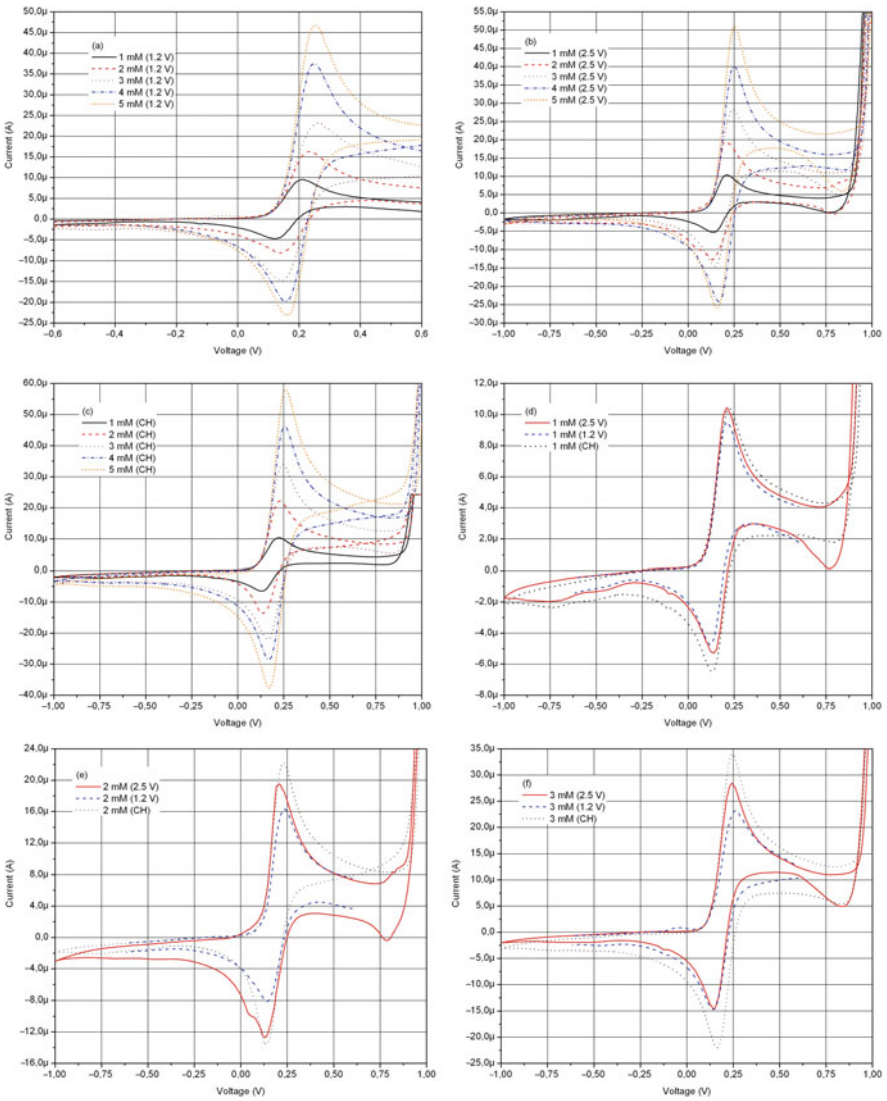

Fig. 3.16 Cyclic voltammetry behavior of the integrated potentiostats (1.2 and 2.5 V) and the commercial instrument CH 1232A with the AC1.W1.R1 sensor and five concentrations (1, 2, 3, 4 and 5 mM) of $K_4[Fe(CN)]_6$ in PBS using a scan rate of 0.05 V/s. (**a**) voltammograms obtained with the 1.2 V Potentiostat Amplifier (PA) for all concentrations, (**b**) voltammograms obtained with the 2.5 V PA for all concentrations, (**c**) voltammograms obtained with the CH instrument for all concentrations. Waveform comparison between the integrated and the commercial potentiostats for all concentrations: (**d**) 1 mM, (**e**) 2 mM, (**f**) 3 mM, (**g**) 4 mM and (**h**) 5 mM

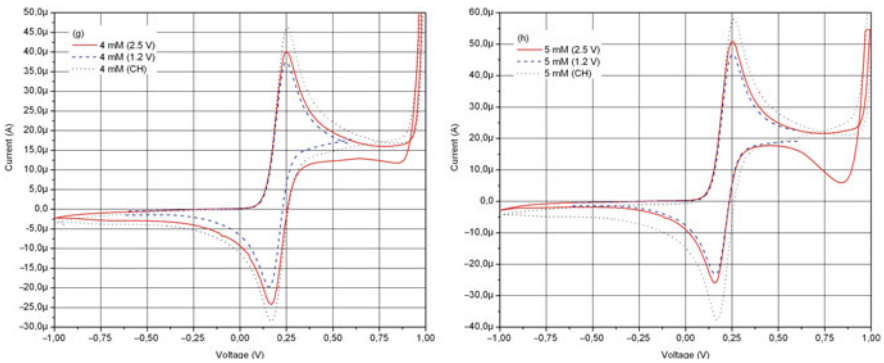

Fig. 3.16 (continued)

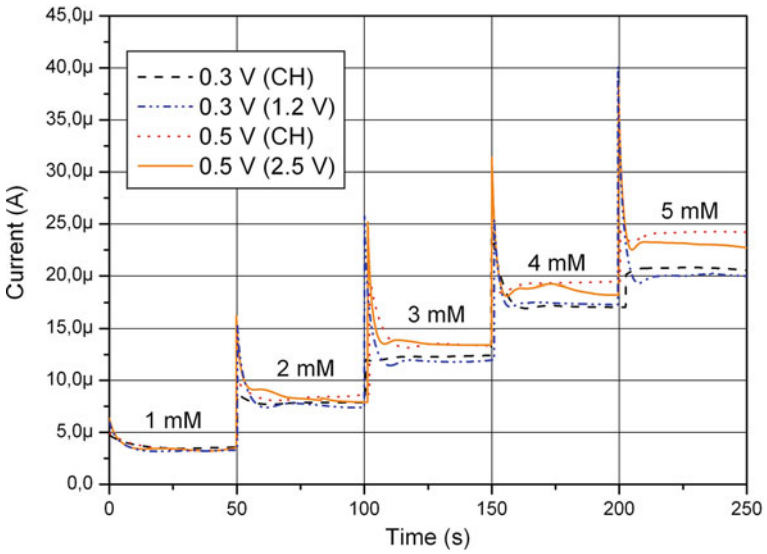

Fig. 3.17 Amperogram recorded during the electrochemical reaction of 1, 2, 3, 4 and 5 mM of $K_4[Fe(CN)]_6$ in PBS for the three potentiostats. The applied cell voltage is 0.5 V for the 2.5 V integrated potentiostat and 0.3 V for the 1.2 V potentiostat. The amperometries are compared with the ones obtained by the commercial instrument CH 1232A (CH)

For the 2.5 V integrated potentiostat a potential of 0.5 V is applied to the amperometry whereas for the 1.2 V potentiostat a voltage of 0.3 V is used. The obtained amperograms are presented in Fig. 3.17 where can be compared with the ones obtained with the CH 1232A. In that case, the results are similar between the commercial and the full-custom integrated potentiostats. The current peaks are produced when the new concentration is added to the solution. They can be reduced using a low pass filter in order to avoid them in the design of some applications.

Finally, Table 3.5 summarizes the hardware specification for each designed integrated potentiostat.

Table 3.5 2.5 and 1.2 V potentiostats hardware specifications

Symbol	Parameter	Value		Units
V_{CC}	Power voltage	1.2 (±0.6)	2.5 (±1.2)	V
Potential[a]	V_{Cell} voltage	1 (±0.5)	2 (±1)	V
Max. current	Max. current detected	±1	±1	mA
Min. current	Min. current detected	±1	±0.1	nA
Freq.	Max. working freq.	2,000	8,000	Hz
P_{CC}	Power consumption	240	580	μW
Size	W × L	1,700 × 900	300 × 250	μm × μm

[a]Voltage across *Reference* and *Working* electrodes

3.4 Low-Frequency Lock-In Amplifier

As previously commented, in some cases the sensor gives the information about the electrochemical reaction by modification on its impedance [28]. Not a full Electromechanical Impedance Spectroscopy (EIS) is carried out and a variation of the Biosensor impedance (or capacitance) is just sensed at one or various defined frequencies where the sensor is more sensitive to changes on the analyte concentration [62]. In those cases, a specific electronics able to evaluate the complex value of impedance is necessary.

Label free impedance Biosensors can detect a great variety of targets, like proteins, DNA, small molecule sensors [63], cell-based Biosensors [62, 64], etc. Due to their low cost, low power and ease of miniaturization, electrical Biosensors hold great promise for applications where minimizing size and cost is crucial, such as point-of-care diagnostics, biological warfare agent detection and integrated in-vivo point-of-care detectors.

The signals to be measured have often very small amplitude and they are usually in a very noisy environment. Then, it is mandatory to extract the signal from the noise and a very promising approach is based on the use of a lock-in amplifier [65] capable to identify the real and imaginary parts of the complex impedance while reducing the effect of the noise [66, 67].

Looking for this kind of implementations, there is a trade-off between complexity, area, power consumption, with the desired measurements and the electronic implementation. In that way, a fully-integrated DSP solution, as a digital lock-in amplifier, would present a big challenge to develop an implantable low power device. Obviously, commercial lock-in amplifiers are costly and large, and they are not suitable for portable electronics.

A miniaturized solution based on an analog lock-in amplifier module has to be designed in order to measure impedances associated with the analysis of biological cells, in the frequency range of interest. A digital solution is not developed due to its large silicon area needed in the integrated implementation and its higher power dissipation compared with a full-custom analog solution.

Following this assumption it is designed (schematic and layout level) an analog lock-in amplifier as an electronic interface for implantable low frequency Biosensors applications. The presented design looks for a very small power consumption working at very low power supply (1.2 V).

3.4.1 Lock-In Amplifier Architecture

The impedance detection [68] is carried out by introducing an AC signal to the sensor; hence an AC signal is obtained in the sensor output. In that way, when working with amperometric sensors, an AC output current is obtained and the impedance could be defined as the division between the input AC voltage and the output current.

The input voltage is applied to the three electrodes Biosensors using the control module presented in Section 3.3.1. On the other hand, a transimpedance amplifier converts the output AC current into a proportional voltage as it is detailed in Section 3.3.2. At that point, it is introduced the lock-in circuit to detect the real and imaginary parts of the impedance. Figure 3.18a presents the block diagram structure of the impedance analyzer instrument.

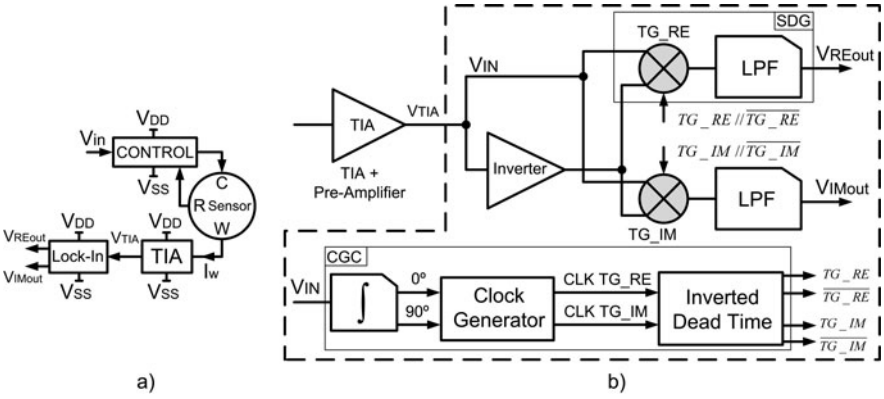

Fig. 3.18 (**a**) Lock-in module position in the potentiostat structure and (**b**) Lock-in amplifier block diagram

The integrated lock-in is based on two Synchronous Demodulated Channels (SDG) and a Clock Generation Circuit (CGC), Fig. 3.18b. Both channels are used to find, at the same time, two DC components that are related with the real and imaginary values related with the Biosensors. The Front-End is composed by an input pre-amplifier used to feed the incoming signal from the I-V converter to the voltage accepted by the channels. On the other hand, the Back-End demodulation is formed by an inverter amplifier, two Low Pass Filters (LPF) and two transmission gates (TG) [69]. This TG demodulator acts as a multiplier.

The adopted Pre-Amplifier configuration is a wide-swing, rail-to-rail output stage with feedforward class-AB control [66, 67] presented in Fig. 3.7 with a

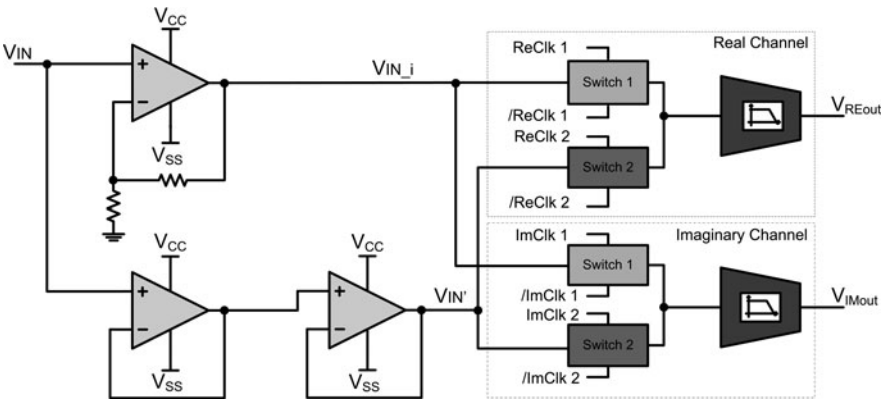

Fig. 3.19 Back-end implementation of the synchronous demodulated channels (SDC)

gain-bandwidth product of 300 kHz for a load capacitor of 20 pF. This pre-amplification is included in the I-V conversion stage.

The demodulator is a multiplier. It takes the input and the reference signals and multiplies them together. When you multiply two waveforms together you get the sum and difference frequencies as a result. Since the input signal and the reference signal are of the same frequency, the difference frequency is zero and you get a DC output which is proportional to the amplitude of the input signal and the cosine of the phase difference between the signals.

By adjusting the phase of the reference signal using the reference circuit, the phase difference between the input signal and the reference can be brought to zero and hence the DC output level from the multiplier is proportional to the input signal.

The Back-end implementation of the Lock-In amplifier is presented in Fig. 3.19 with the inverter and the real and imaginary channels. Furthermore, two voltage followers are included in the non-inverted line to compensate the delay error between channels. Both, the inverter and the follower, use the same previous class AB amplifier.

The Clock Generation Circuit generates the 4 clock signals for the transmission gates (TG) with the same AC signal used to drive the electrochemical cell, Fig. 3.18. Hence, this four clocking scheme defines the on/off state of the analog TG's for a synchronous rectification. Moreover, a Dead Time generation is introduced to reduce the clock feed-through noise [70] as well as, a dummy half size transistor to cancel the charge injection errors.

The first step in the Clock Generation scheme consists on generating a 90% delayed signal from the input ones. This means that the real channel reference clocks are based on a sinus waveform whereas the imaginary channel is controlled by a cosines signal obtained by integration of the original sinus signal.

The 0 and 90° signals are obtained following the architecture depicted in Fig. 3.20. Since a low frequency operation is expected, a classical integration topology based on a class AB operational amplifier is chosen. Its transfer function is

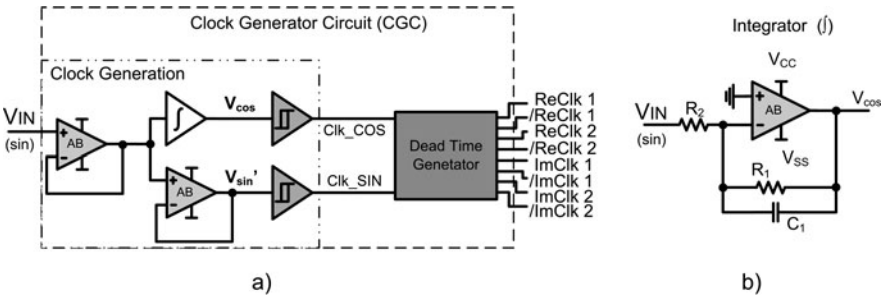

Fig. 3.20 (**a**) Clock generation circuit architecture and (**b**) Integrator topology

defined in Eq. (3.9). Moreover, Eq. (3.10) has to be maintained to guaranty the best integration ratio as well as a unitary gain.

$$H(s) = -\frac{R_1/R_2}{sC_1R_1 + 1} \tag{3.12}$$

$$Z_1 = Z_2 \Rightarrow R_2 = (C_1 \,\|R_1) \tag{3.13}$$

Two important remarks when using this kind of integrators: First, capacitor C_1 has to be pre-charged during the start-up and second, it must be stated that the impedance should be matched so, if the frequency presents a huge range variation, the capacitor C_1 should be changed or other solution must be adopted. Just as in the Back-end, a voltage follower is introduced to compensate the delay produced by the integrator.

Moreover, an extra follower is added at the beginning of the Clock Generator to compensate the delay between the clock generation and the Back-End stage. In that way, all generated on-chip signals present the same delay so, the final error is reduced.

The last step consists on generating the square clock signal from the 0 and 90% sinus waveforms. This is accomplished by using comparators based on the structure presented in Fig. 2.45, Section 2.3.3.2. Figure 3.21 shows the two clock generated signals and the delay between them. It is compensated by adding followers in the Clock Generator circuit and in the Back-End stage.

Later, the two out of phase signals are introduced in the Dead Time Generator to drive properly the CMOS Transmission Gates with four non-overlapped clock signals per channel. Also, dummy half size transistors have been used to cancel the charge injection errors.

Then, the two signals coming from the Transmission Gate rectifiers are filtered through two active low-pass filters (Section 3.4.3) thus, two DC components are obtained, V_{REout} and V_{IMout}, one per each channel. Finally, the magnitude and phase of the impedance are obtained afterwards combining both DC values using Eqs. (3.11) and (3.12).

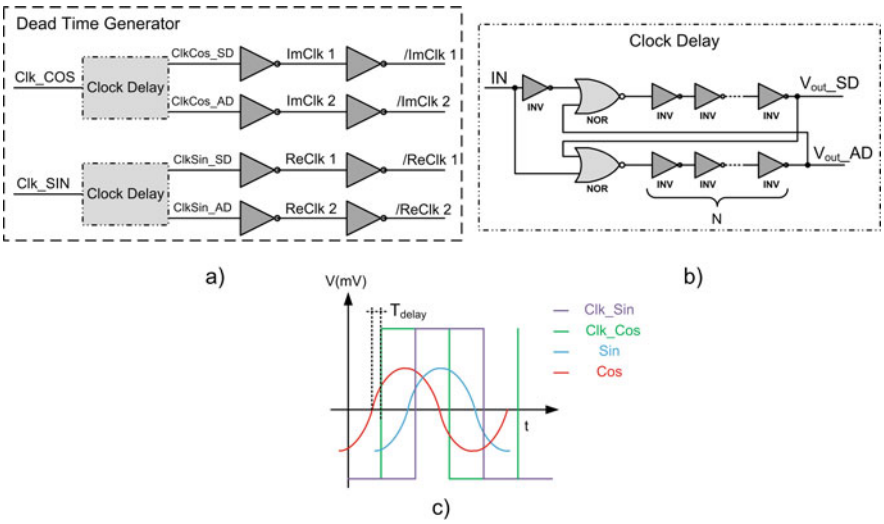

Fig. 3.21 (**a**) Dead time generation structure, (**b**) detailed schematic of the delay generation and (**c**) illustration of delay operation

$$Magnitude = \sqrt{V_{REout}^2 + V_{IMout}^2} \tag{3.14}$$

$$Phase = Tan^{-1}\left(V_{IMout}/V_{REout}\right) \tag{3.15}$$

3.4.2 Lock-In Simulation Results

The performance of the lock-in amplifier is analyzed using the extracted views of the circuitry. An ideal AC signal is used to define the input sinusoidal module and phase (V_{IN}). Fixed amplitude of 60 mV is selected whereas the phase is changed between different values.

Regarding the two DC voltage levels at the output of the filters, V_{REout} and V_{IMout}, the theoretical amplitude and phase are compared with the calculated values using Eqs. (3.11) and (3.12), for a particular frequency of 10 kHz. A maximum error of a 2% is obtained in the Amplitude measurement (A_{ERR}).

Figure 3.22 depicts the Phase simulated values compared with the theoretical ones. In that case, an error around 1% (P_{ERR}) is achieved. Both error values, M_{ERR} and P_{ERR}, are good results taking into account the reported errors by the commercial SR830 lock-in amplifier by Stanford Research Systems©, which presents an Amplitude error (A_{ERR}) around 2.29% @ 10 kHz, as a reference [43].

Table 3.6 presents the simulated performance of the lock-in amplifier when there is some noise applied at the input signal of 60 mV. The table shows the obtained DC

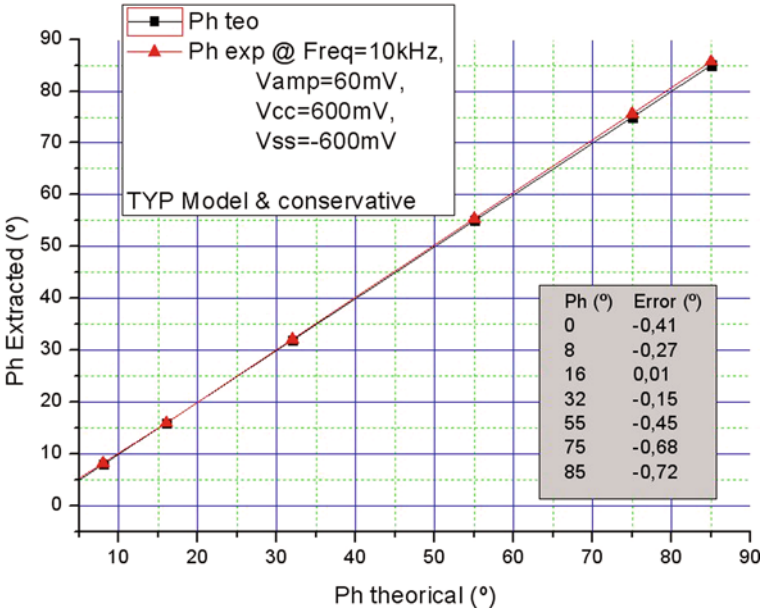

Fig. 3.22 Phase comparison between the calculated (Ph teo) and the simulated (Ph exp) results

Table 3.6 Simulated DC magnitude (V_M) and Phase (φ) obtained with the lock-in amplifier when different noise levels are applied at the input signal of 60 mV @ 10 kHz, $V_{cc} = 1.2$ V. (φ_{teo} (°) = theoretical phase; V_{noise} = noise amplitude; F_{noise} = noise frequency; $|V_M|$ = magnitude, Eq. (3.11); $\epsilon|V_M|$ = magnitude error; φ_{exp} = phase, Eq. (3.12); $\epsilon\varphi_{exp}$ = phase error)

φ_{teo} (°)	V_{noise} (mV)	F_{noise} (Hz)	$\lvert V_M\rvert$ (mV)	$\epsilon\lvert V_M\rvert$ (mV)	φ_{exp} (°)	$\epsilon\varphi_{exp}$ (°)
0	5	500	59.89	0.11	1.1	1.1
45	5	500	59.52	0.48	44.79	0.21
0	100	500	59.86	0.14	1.13	1.13
45	100	500	59.2	0.8	44.99	0.01
0	5	15 k	59.88	0.12	1.1	1.1
45	5	15 k	59.06	0.94	44.92	0.08
0	100	15 k	59.98	0.02	1.11	1.11
45	100	15 k	59.04	0.96	45.47	0.47

value of the Magnitude, Eq. (3.11), the Phase, Eq. (3.12), and the error produced in the detection of both magnitudes.

The total power consumption of the lock-in amplifier is 715 μW for a power supply of ±0,6 V. Table 3.7 presents the consumption for different input amplitude voltages and power conditions whereas Table 3.8 summarizes the most important electrical characteristics of the designed lock-in amplifier.

Table 3.7 Lock-in amplifier power consumption in function of several input voltages amplitudes and power supply voltages

Input (10 kHz)		
V_{Supply}(V)	V_{IN}(mV)	Power (W)
±0.6 V	60	714 μ
±0.6 V	100	713 μ
±1.25 V	60	1.2 m
±1.25 V	100	1.2 m

Table 3.8 Lock-in amplifier maximum values

Symbol	Parameter		Value	Units
V_{CC}	Power voltage	1.2 (±0.6)	2.5 (±1.2)	V
V_{IN}	Maximum input voltage	0.6 (±0.3)	1.2 (±0.6)	V
Freq	Maximum input frequency	10	10	kHz
$\epsilon\|V_M\|$	Magnitude error	2	1.7	%
$\epsilon\varphi_{exp}$	Phase error	1.2	1.03	%
P_{CC}	Power consumption	715	1,200	μW

3.4.3 Active Low-Pass Filter

Two active low-pass filters are used as a last step of the previous Lock-In amplifier architecture. They filter any kind of noise and high frequency interferences in order to reduce errors in the obtained DC signals.

Since the integrated filter must present a very low cut-off frequency, ranging from 0.1 to 30 Hz, some classical solutions like Sallen-Key filter could not be adapted because high values of resistances and capacitances are necessary and then, the IC integration is not possible. A gm-C second-order LP filter is adopted to accomplish the frequency requirements and to be able to integrate the necessary capacitors values.

The final implementation uses a degenerated transconductance amplifier (OTA) to define the *gm* of the filter [71]. This architecture allows defining small transconductance values in the range of few nS [47, 54].

Figure 3.23 shows the schematic of the implemented OTA as well as the in/out current relation. The source degeneration increases the input range of the amplifier and also decreases the equivalent transconductance.

The ratio (M:N) between the current mirrors decreases the current level at the output, which results in an even minor value [72]. These current mirrors are based on composite transistors, used to reach greater copy factors.

Important remarks must be followed when designing this type of current mirrors in terms of layout. A better matching is achieved with techniques like common centroid geometry and with multifingers because large numbers of unit transistors are matched together. Figure 3.24 depicts the OTA's layout.

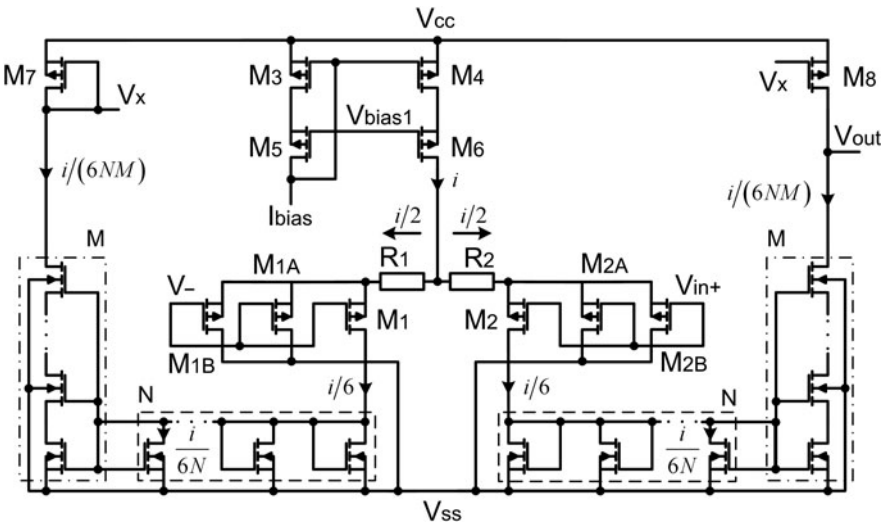

Fig. 3.23 Schematic of the degenerated OTA used to design active filters. Resistors R_1 and R_2 and the M:N ratio between transistors is used to reduce the current at the output stage

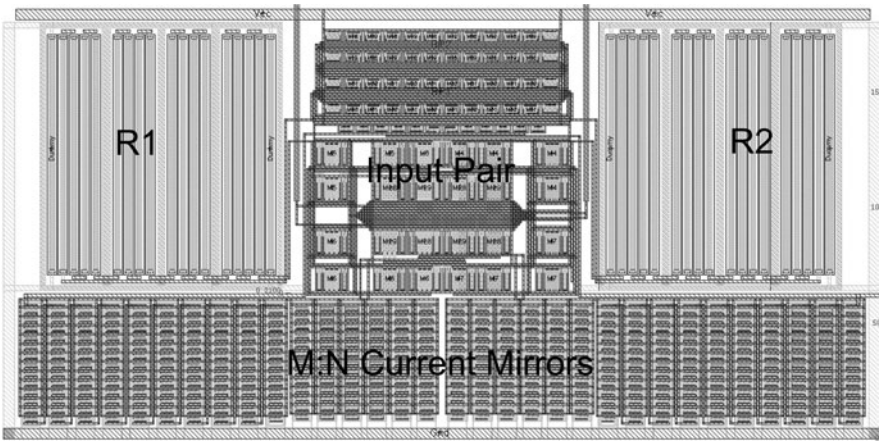

Fig. 3.24 Degenerated OTA layout

The equivalent transconductance (*gm*) for this amplifier is 4.25 nS, for an input range up to ±400 mV and a supply voltage of 1.2 V. The OTA amplifier presents an input offset <1 mV, a THD of 0.03%, and a power consumption around 0.5 μW, for the typical case (TYP Model).

A lower nominal transconductance value up to 1 nS could be achieved. The minimum *gm* value is limited by the leakage currents off each current mirror branch. Table 3.9 summarizes the OTA electrical specifications.

Table 3.9 Degenerated OTA electrical features

Symbol	Parameter	Value		Units
V_{CC}	Power voltage	1.2 (±0.6)	2.5 (±1.2)	V
V_{Offset}	Offset voltage	770.1	–982.54	μV
V_{in}	Input voltage range	0.8 (0.4)	1.9 (1)	V
F_{3db}	Cut-off frequency	32.95	43.39	Hz
g_m	Transconductance	4.241	4.487	nS
THD	Total harmonic distortion	0.273	0.0073	%
I_{CC}	Current consumption	480.4	570	nA
P_{CC}	Power consumption	582.76	1,124.36	nW
Area	W × L	380 × 186		μm × μm

The basic structure of the 2nd order filter is depicted in Fig. 3.25. It is formed by two OTA amplifiers (*gm1*, *gm2*) and 2 capacitors. Its transfer function is defined by Eq. (3.13) where $V_A = V_{IN}$ and $V_B = V_C = 0$ V whereas the cut-off frequency (ω_O) is described by Eq. (3.14) where $gm_1 = gm_2 = gm_2$.

$$Vout = \frac{s^2 C_1 C_2 V_C + sC_1 gm_2 V_B + gm_1 gm_2 V_A}{s^2 C_1 C_2 + sC_1 gm_2 + gm_1 gm_2} \tag{3.16}$$

$$\omega_O = \frac{gm}{\sqrt{C_1\ C_2}} \tag{3.17}$$

An important factor to define the selectivity of the filter is the Quality factor (Q) that is described as the resonant frequency (f_0) divided by the bandwidth ($f–f_2$) [73]. The higher the Q, the higher the selectivity resulting in a bandwidth decrement of the filter. In that specific design, looking for low cut-off frequencies, high values of selectivity could be achieved following Eq. (3.15).

$$Q = \frac{f_0}{f_2 - f_1} = \frac{f_0}{\Delta f} = \sqrt{\frac{C_2}{C_1}} \tag{3.18}$$

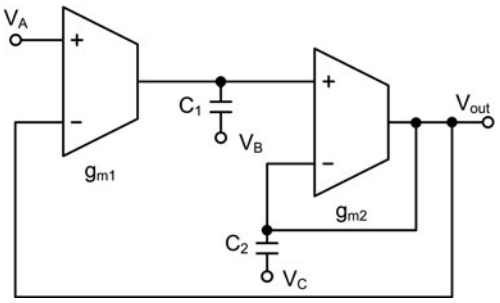

Fig. 3.25 2nd order gm-filter based on OTA amplifiers

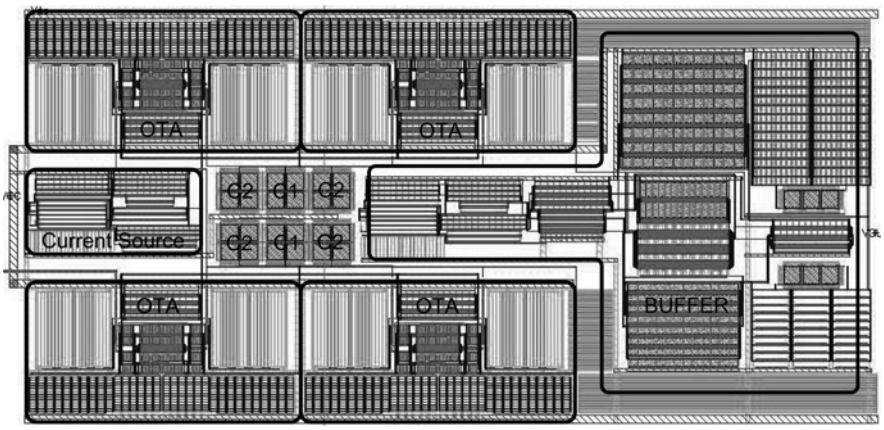

Fig. 3.26 Layout of the 4th order filter based on OTA amplifiers

For a quality factor Q of 0.7 is derived that $C_2 = 2\ C_1$ because in that design $gm_1 = gm_2 = gm$ [73]. For a cut-off frequency of 3 Hz, and $gm = 4.25$ nS, then $C_1 = 100$ pF and $C_2 = 200$ pF. These are huge values to be integrated. Then, for a test approach, $C_1 = 10$ pF has been adopted defining a cut-off frequency of 47 Hz.

Moreover, a four-order filter is designed connecting in cascade two 2nd order filters. It presents a better frequency response and roll-off decay, but in terms of area and power dissipation, it has been considered to define a cut-off frequency around 30 Hz and a $C_1 = 10$ pF. This filter has a power consumption of 50 μW, and a size of 770 μm × 575 μm. Figure 3.26 shows the layout of the 4th order LP filter. The second order filter follows the same structure with just two integrated OTA's. Finally Table 3.10 summarizes the experimental electrical features for both filters.

Table 3.10 2nd and 4th order filter characteristics

	Parameter	Value				
Filter	Type of filter	2nd order		4th order		
V_{CC}	Power voltage	1.2 (±0.6)	2.5 (±1.2)	1.2 (±0.6)	2.5 (±1.2)	V
V_{in}	Input voltage	0.8 (0.4)	1.9 (1)	0.8 (0.4)	1.9 (1)	V
F_{3db}	Cut-off freq.	47.4	49.34	31.95	23.18	Hz
g_m		4.241	4.487	4.241	4.487	nS
BP	Attenuation	>40	>60	>80	>80	dB
P_{CC}	Consumption	1.12	1.9	2.3	3.96	μW
Area	L × W (μm)	400	560	775	570	

3.5 Biotelemetry for Implanted Devices

Biotelemetry [2, 74–76] consists of transmitting the information obtained from the patient to the signal processing or reception unit using a wireless link. This technique is used in some medical instruments, like in ECG [77], in order to monitor

a patient while giving full mobility to the subject. Moreover, this is one of the best methods to isolate the patient from the power lines avoiding the risk of electric shocks.

The transmission of the information is an important challenge to solve for those implanted devices under the human skin and, Biotelemetry, is one of the most suitable techniques to establish a communication between the internal detection unit, under the human skin, and the external reader.

Solutions based on wires are also studied in the bibliography but they present some technical problems, like possible infections and the inconvenience of wearing wires through the skin, and nowadays are not widely used.

Two types of Implantable devices can be distinguished: the first ones known as monitor devices [78] and the second ones known as detection devices [79].

Monitor consists on sending continuously information about the state of the patient or about the substance to be analyzed to the external reader. On the other hand, detection devices just send information about specific important points of the state of the subject or substance.

I.e. in a monitoring device the glucose is sensed continuously and the results are transmitted also continuously or periodically [80, 81]. If a detection device is used, the glucose is sensed continuously but just some important threshold values are transmitted. So, two types of data transmission modes can be defined depending on the type of the implantable device:

- Mode RAW/CONTINUOUS data transmission:

It is used in Monitor devices because it allows high data rates, lots of bidirectional information can be transmitted continuously. Normally, it uses an extra dedicated antenna for communication because the transmission frequency is higher than the used for inductive powering (Fig. 3.27).

It implements complex analog and digital modulation mechanisms [82] in order to send as much information as possible. Furthermore, time and frequency multiplexing of several signals is also possible [83]. The main disadvantage regards the high power levels required for the transmission and processing. Specific low power circuits like receivers, emitters, transponders [84] ... have to be developed specifically for implantable devices [85, 86] to avoid problems regarding thermal transference with the biological tissue around it.

- Mode SINGLE data transmission:

It consists in sending small amount of information, just some bits or bytes. The idea is to transmit the necessary data to advice the external unit about some specific point (or points) with medical interest.

Since the transmitted data rate is low it is possible to use as a carrier frequency the same as the one used for the inductive powering [87] then, a modulation method called backscattering could be used.

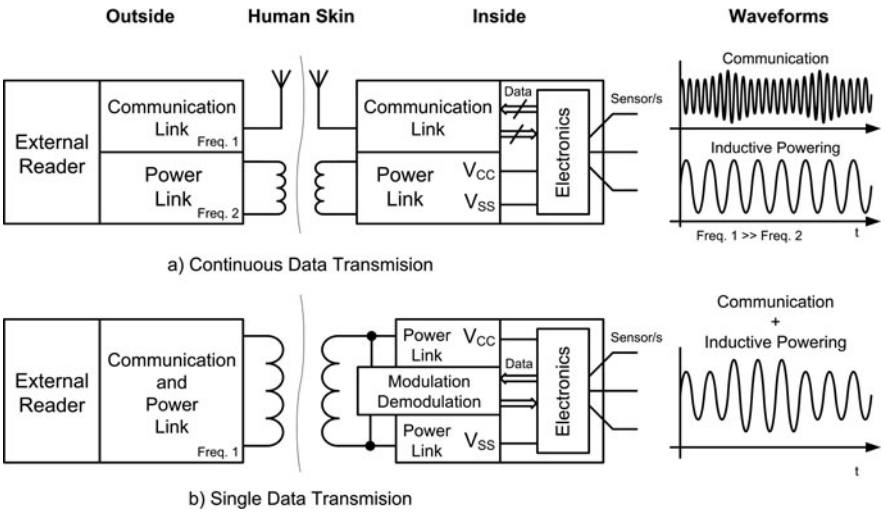

Fig. 3.27 Continuous and single communication data methods block diagram

It consists in modifying the inductive coupling between the primary and remote coil. The transmission could be done in both directions, from the primary to the secondary coil by modulating the magnetic field, and in the opposite direction changing the impedance, tuning frequency or power consumption of the secondary coil. In that way, a variation in the induced secondary coil magnetic field produces a variation of the primary coil voltage defining an AM modulation as seen in Fig. 2.27.

The circuits involved on this kind of transmission are less complex than the ones used in the continuous mode, therefore the involved power is also smaller. This is an important reason to select that mode to develop detection implantable devices. Moreover, the simple procedure for data communication using the same magnetic field created by the power transmission coils is an extra added value for implantable devices in order to reduce the total size of the device and to reduce the impact in its biological environment.

3.5.1 Low-Power Single Data Transmission Protocol

As it is introduced a Single Data Transmission consists in just sending some specific points of the evaluated data. The implemented transmission approach uses a comparator block able to detect three different threshold points and a monostable [88] based circuit to transmit the data.

The block diagram of the communication module is presented in Fig. 3.28. It is formed by 5 sub circuits, a threshold generator circuit (Vth Gen.), a low-pass filter (LPF), a Comparator Module, a DC Modulation and a monostable based circuit. The low pass filter (LPF) is used to reduce the noise in the input voltage. Then, the

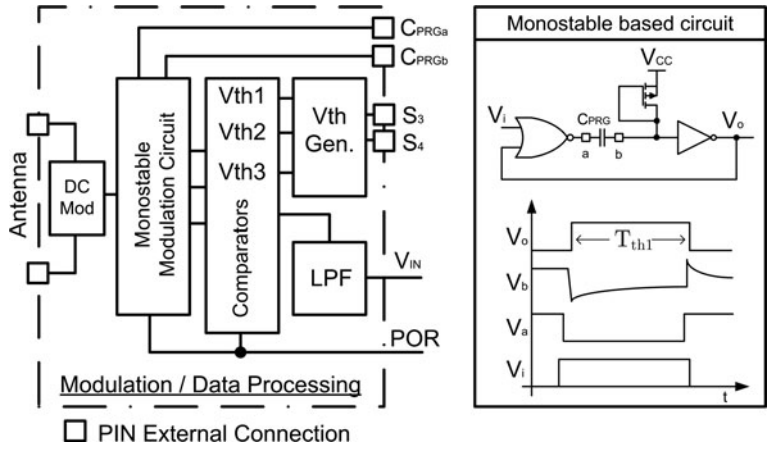

Fig. 3.28 Modulation/data processing block diagram

filtered signal is introduced to the comparator circuit where the threshold points are detected (interesting points).

Later on, and depending on the result of the comparison, the Modulation Circuit activates the modulation through the DC switch. The internal threshold voltages are generated on-chip and could be selected using signals S_3 and S_4.

The designed LPF is based on the 2nd order OTA filter presented in Section 3.4.3 with a cut off frequency of 50 Hz. The filter reduces problems regarding glitches and fast transient noise signals avoiding problems in the level detection. It reduces the risk of transmitting false positives to the main station.

The AM communication is done following the idea presented in Fig. 3.29. The circuit monitors the incoming voltage V_{IN} and, in function of three threshold voltages (V_{th1}, V_{th2} and V_{th3}), modulates the amplitude of the signal at the internal antenna.

A Power-On-Reset (POR) signal activates the circuitry when there is enough voltage to drive properly the circuits, start-up time (T_{SUP}), and the antenna starts to transmit continuously a series of ones. At that point, the Modulation/Data Processing unit is prepared to transmit the detected threshold voltages.

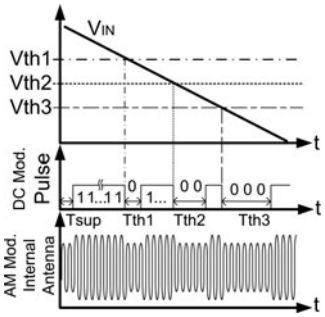

Fig. 3.29 Implemented single data transmission protocol

When the input voltage reaches the first threshold level the system transmits one zero (T_{th1}) to the external reader. Two zeros are transmitted (T_{th2}) if the second comparator threshold value is reached by V_{IN}. Finally, when the third is achieved a series of three zeros are sent (T_{th3}). Several on-chip threshold voltages could be selected using S_3 and S_4 (Section 4.2.7).

A default zero time slot interval is defined as 250 ms ($T_{th1} = 250$ ms). This time is controlled by an external capacitor, C_{PRG}, connected in the monostable based circuit. The time slot is controlled by the charging time of the C_{PRG} defined as

$$C_{PRG} \cdot \Delta V = I \cdot \Delta T \tag{3.19}$$

where I is the current injected to the capacitor by the diode connected transistor (Monostable circuit, Fig. 3.28), ΔV is the defined threshold voltage of 0.8 V used to activate the inverter gate of the monostable circuit and ΔT is the desired time slot used to define a transmitted zero. The time slot (T_{th1}) could be easily modified by changing the value of the capacitor, C_{PRG}. Table 3.11 presents some examples of capacitors and its defined time slot.

Table 3.11 Time slot (T_{th1}) definition using C_{PRG}

I(nA)	ΔV(V)	T_{th1}(ms)	C_{PRG}
1	0.8	125	150 nF
1	0.8	250	320 nF
1	0.8	500	625 nF
1	0.8	750	950 nF
1	0.8	1,000	1.25 μF

The comparisons of the input signal with the threshold voltages are achieved using three low-power comparators. The selected ones are based on the circuit explained in Section 2.3.3.2 (Fig. 2.45) with a reduced hysteresis of 5 mV. The introduction of the hysteresis helps the LPF filter to reduce noise problems with the input signal.

Then, the signals generated by those comparators are used by the logic circuitry to transmit the number of zeros. If more than one zero has to be transmitted, the circuitry re-starts again the monostable circuit. The total power consumption of this block is 1.2 μW. An example of the communication protocol mechanism is presented in Section 4.3.

3.6 Chapter Conclusions

A three electrodes amperometric sensor is formed by the Counter, the *Reference* and the *Working* electrode. It generates a current proportional to the electrochemical reaction that occurs in the W electrode. Different electrochemical techniques, Cyclic

Voltammetry, EIS... can be applied to know the behavior of the reaction for several conditions.

The Potentiostat Amplifier (PA) is the electronic circuit used to deal with the three electrode Biosensors. It is basically formed by two blocks: (1) the Control and (2) the Current Detection Module.

The Control Module regulates the voltage across the *Reference* and *Working* electrodes in order to control perfectly its voltage. This is important for the electrochemical reaction that takes place in the W electrode. Three class AB operational amplifiers have been used to implement this block. On the other hand, the Detection Module is in charge to detect the current generated by the reaction at the *Working* electrode. In this work a transimpedance amplifier is the selected option.

Two low-power potentiostats have been finally integrated on silicon. The first one is designed to work up to 2.5 V or ± 1.2 V, whereas the second one is designed for low-voltage applications with a voltage up to 1.2 V or ± 0.6 V.

Both designs are tested with a commercial three electrodes sensor and with a real electro-active substance, $K_4[Fe(CN)]_6$. The results of several Cyclic Voltammetries and amperograms are compared with the ones obtained with a commercial potentiostat. Thus, it can be assured a perfect operation of the integrated PA in the desired current ranges assuring a lower power consumption and area than the commercial one.

This chapter also introduces the design and conception of a complex impedance detection circuit called Lock-In amplifier. This circuit, theoretically introduced, is based on the use of two Synchronous Demodulated Channels to obtain the real and imaginary parts of the complex impedance. Then, the circuit is validated through several simulations.

Finally, the concept of Biotelemetry is explained and a simple low-power protocol for transcutaneous transmissions is developed. It is based on the backscattering concept that consists in changing the impedance of the implanted coil to modify the coupling factor of the inductive link.

References

1. P.H. King, R.C. Fries, *Design of Biomedical Devices and Systems*, 2nd edn. (CRC Press, Florida, USA, 2009), ISBN: 978-1-4200-6179-6
2. J.G. Webster, Medical Instrumentation Application and Design, 3rd edn. (Wiley, New York, USA, 1998), ISBN: 0-471-15368-0
3. R.P. Areny, *Sensores y Acondicionadores de Señal*. 3ª Edición, (Marcombo, Barcelona, Spain, 1998), ISBN 84-267-1171-5
4. C. Wen-Yaw, P. Arnold, W. Ying-Hsiang, T. Tseng, *A 600 μW Readout Circuit with Potentiostat for Amperometric Chemical Sensors and Glucose Meter Applications*, IEEE Conference on Electron Devices and Solid-State Circuits, EDSSC 2007, 20–22 (2007)
5. F.Z. Padmadinata, J.J. Veerhoek, G.J.A. van Dijk, J.H. Huijsing, Microelectronic skin electrode. Sens. Actuators B Chem. **1**(1–6), 491–494 (1990)
6. L. Ramasamy, *ASIC System Development of MEMS Bio-chip Analyzer with Calibration, Signal Capture and Display Circuit*, (University of Cincinnati, 2005) Available at: http://etd.ohiolink.edu/view.cgi?acc_num=ucin1127337845

7. S.K. Kailasa, S.H. Kang, Microchip-based capillary electrophoresis for DNA analysis in modern biotechnology: A review, Taylor. Francis. Sep. Purif. Rev. **38**, 242–288 (2009)
8. V.M. Ivama, S.H.P. Serrano, Rhodium – Prussian Blue modified carbon paste electrode (Rh – PBMCPE) for amperometric detection of0020hydrogen peroxide. J. Brazilin. Chem. Soc. **14**(4), (Aug 2003). ISSN: 0103–5053
9. X. Ji, C.E. Banks, A. Crossley, R.G. Compton, Oxygenated edge plane sites slow the electron transfer of the ferro-/ferricyanide redox couple at graphite electrodes. Chem. Phys. Chem. **7**, 1337–1344 (2006)
10. F. Heer et al., CMOS microelectrode array for the monitoring of electrogenic cells. Biosens. Bioelecron **20**, 358–366 (2004)
11. S.M. Radke, E.C. Alocilja, A microfabricated biosensor for detecting foodborne bioterrorism agents. IEEE Sens. J. **5**(4), 744–750 (2005)
12. D.L. McCulloch, G.B. Boemel, M.S. Borchert, Comparison of contact lens, foil, fiber, and skin electrodes for patterns electroretinograms. Doc. Ophtalmol **94**, 4 (1997)
13. O. Chailapakul, J. Promnil, M. Somasundrum, M. Tanticharoen, Immobilized K3Fe(CN)6 and glucose oxidase in polypyrrole on a gold micro-electrode and the it application as a glucose sensor. J. Sci. Res. Chula. Unit. **25**, 1 (2006)
14. S.V. Dzyadevych et al., Electrochem. Enzyme. Biosens. (2006). ISBN: 966-02-4200-X
15. F. Mizutani, E. Yamanaka, Y. Tanabe, K. Tsuda, An enzyme electrode for L-lactate with chemically amplified electrode. Anal. Chem. Acta. **117**, 153–166 (1985)
16. P.N. Bartlett, R.G. Whitaker, Strategies for the development of amperometric enzyme electrodes. Biosensors **3**, 359–379 (1987)
17. L.E. Morrison, Time resolved detection of energy transfer: Theory and application to immunoassays. Anal. Biochem. **174**, 101–120 (1988)
18. H.A. Lee, M.R.A. Morgan, Food immunoassay: Application of polyclonal, monoclonal and remobinant antibodies. Trends Food Sci. Technol. **3**, 129–134 (1993)
19. C. Dumschat et al., Pesticide-sensitive ISFET based on enzyme inhibition. Anal. Chim. Acta. **252**, 7–9 (1991)
20. P. Bergveld, Thirty years of ISFETOLOGY. What happened in the past 30 years and what may happen in the next 30 years. Sens. Actuators B **88**, 1–20 (2003)
21. E. Lorenzo et al., Analytical strategies for amperometric biosensors based on chemically modified electrodes. Biosens. Bioelectron **13**, 319–332 (1998)
22. D.B. Kell, C.L. Dave, *Conductimetric and Impediometric Devices in Biosensors. A Practical Approach*, (IRL Press, Oxford, 1990)
23. D.C. Cullen et al., Multi-analyte miniature conductance biosensor. Anal. Chim. Acta. **231**, 33–40 (1990)
24. J. Colomer-Farrarons, P. Miribel-Català, A. Saiz-Vela, J. Samitier, in *Proceeding of the 16th IEEE International Conference on Very Large Scale Integration VLSI – SOC*, A 50 μW low-voltage CMOS Biopotentiostat for low frequency Capacitive Biosensor, 2008
25. A. Gore, S. Chakrabartty, S. Pal, E. Alocilja, A multi-channel femtoampere-sensitivity conductometric array for biosensing applications. IEEE Transactions on Circuits and Systems I: Regular Papers, **53**(11), 2357–2363 (2006)
26. L.Y. Woo, L.P. Martin, R. Glass, R.J. Gorte. Impedance characterization of a model Au/Yttria-Stabilized Zirconia/Au electrochemical cell in variying oxygen and NOx concentrations. J. Electrochem. Soc. **154**(4), 129–135 (2007)
27. J.M. Flores, R.D. Romero, J.G. Llongueras, Espectroscopía de impedancia electroquímica en corrosión, Instituto Mexicano del Petróleo, UNAM, Available at: depa.pquim.unam.mx/labcorr/libro/Manual-EIS-IMP-UNAM.PDF
28. A. Lasia. *Electrochemical Impedance Spectroscopy and Its Applications. Modern Aspects of Electrochemistry*, vol. 32. (Kluwer Academic/Plenum Publisher, New York, USA, 1999), Chapter 2, p. 143

29. R.J. Reay, S.P. Kounaves, G.T.A. Kovacs, An integrated CMOS potentiostat for miniaturized electroanalytical instrumentation, IEEE International 41st ISSCC Solid-State Circuits Conference, pp. 162–163 (1994)
30. C. Berggren, B. Bjarnason, G. Johansson, Capacitive biosensors, Electroanalysis **13**(3), 173–180 (2001)
31. S. Grimnes, O.G. *Martinsen, Bioimpedance and Bioelectricity Basics*, 2nd edn. (Academic Press, Elseiver, London, UK, 2008). ISBN: 0-12-303260-1
32. Diffusion Element, http://www.consultrsr.com/resources/eis/diffusion.htm
33. M.N. Latto, *The Electrochemistery of Diamon*, (University of Bristol, Bristol, UK, Sep 2001), http://www.chm.bris.ac.uk/pt/diamond/mattthesis/contents.htm
34. C.G. Zoski, *Handbook of Electrochemistery*, (Elsevier, The Netherlands, 2007), ISBN: 0-444-51958-0
35. Cypress Systems Cyclic Voltammetry, http://www.cypresssystems.com/Experiments/cv.html Amperometri
36. GAMRY Instruments App. Note, Electrochemical Impedance Spectroscopy, http://www.gamry.com/App_Notes/EIS_Primer/EIS_Primer.htm
37. J. Braz, Rhodium–prussian blue modified carbon paste electrode (Rh-PBMCPE) for amperometric detection of hydrogen peroxide. J. Brazilian Chem. Soc. **14**, 4 (2003). ISSN 0103–5053
38. A.J. Bard, L.R. Faulkner, *Electrochemical Methods. Fundamentals and Applications*, 2nd edn. (Wiley, New York, NY, 2001). ISBN 0-471-04372-9
39. S.M. Martin, F.H. Gebara, T.D. Strong, R.B. Brown, A low.voltage, chemical sensor interface for system-on-chip: The fully-differential potentiostat, Proceeding of the 2004 International Symposium on Circuits and Systeems ISCAS'02, vol. 4, pp. IV–892–895, (2004)
40. E. Lauwers, J. Suls, W. Gumbrecht, D. Maes, G. Gielen, W. Sansen, A CMOS multiparameter biochemical microsensor with temperature control and signal interfacing. IEEE J. Solid-State Circuits **36**, 12 (2001)
41. S.M.R. Hasan, Stability analysis and novel compensation of a CMOS current-feedback potentiostat circuit for electrochemical sensors. Sens. J. IEEE. **7**(5), 814–824 (May 2007)
42. J. Colomer-Farrarons, P. Miribel-Català, A. Saiz-Vela, I. Rodriguez, J. Samitier, in *Proceedings of the IEEE MWSCAS Conference*, A low power CMOS Biopotentiostat in a Low-Voltage 0.13 μm Digital technology, Cancún, Mexico, 2009
43. J. Colomer-Farrarons, P. Miribel-Català, I. Rodriguez, J. Samitier, in *Proceedings of the XX IECON Conference*, CMOS Front-end Architecture for In-Vivo Biomedical Implantable devices, Porto, Portugal, 2009
44. J. Colomer-Farrarons, P. Miribel-Català, A. Saiz-Vela, M. Puig, J. Samitier, A. Errachid, A 50 μW low-voltage CMOS Biopotentiostat for low-frequenciy Capacitive Biosensor, Proceedings of the XX IEEE VLSI Conference, Rhodes, Greece, 2008
45. S.M. Martin, F.H. Gebara, B.J. Larivee, R.B. Brown, A CMOS-integrated microinstrument for trace detection of heavy metals. IEEE J. Solid-State Circuits **40**(12), 2777–2786 (2005)
46. T.D. Strong, S.M. Martin, R.F. Franklin, R.B. Brown, in *Proceedings of the IEEE International Symposium on Circuits and Systems*, Integrated electrochemical neurosensors, 2006, pp. 4110–4113
47. R. Jacob Baker, *CMOS: Circuit Design, Layout, and Simulation*, Revised 2nd edn. (Wiley – Interscience, NJ, USA, 2008). ISBN 978–0-470-22941-5
48. R. Gregorian, *Introduction to CMOS Op-Amps and Comparators*, (Wiley, New York, USA, 1999). ISBN 0-471-31778-0
49. J.H. Huijsing, *Operational Amplifiers, Theory and Design*, (Kluwer Academic Publishers, Dordrecht, The Netherlands, 2001). ISBN: 0-7923-7284-0
50. F. Maloberti, *Analog Design for CMOS VLSI Systems*, (Kluwer Academic Publishers, The Netherlands, 2001). ISBN: 0-7923-7550-5

51. A.C. Patil, F. Xiao, M. Mehregany, S.L. Garverick, Fully-monolithic, 600°C differential amplifier in 6H-SiC JFET IC technology, Custom Integrated Circuits Conference, CICC'09, pp. 73–76, (2009)
52. J.P. Close, F. Santos, in *Proceeding of the Bipolar/BiCMOS Circuits and Technology Meeting*. A JFET input single supply operational amplifier with rail-to-rail output, pp. 149–152, (1993)
53. F. Serra-Graells, A. Rueda, J.L. Huertas, *Low-Voltage CMOS Log Companding Analog Design*, (Springer, Netherlands, 2003). ISBN: 978-1-4020-7445-5
54. R.J. Baker, *CMOS: Mixed-Signal Circuit Design*, 2nd edn. (Wiley – IEEE Press Series on Microelectronic Systems, NJ, USA, 2008). ISBN: 978-0-470-29026-2
55. National Instruments, Lab View software, http://www.ni.com/labview/
56. X. Gan, Y. Wu, L. Liu, W. Hu, Effects of $K_4Fe(CN)_6$ on electroless copper plating using hypophospite as reducing agent. J. Appl. Electrochem. **37**, 899–904 (Springer, Apr 2007)
57. CH Instruments, http://www.chinstruments.com/
58. BVT Technologies, http://www.bvt.cz/
59. N.I. Bojorge Ramírez, M.Fortes, A.M. Salgado, B. Valdman, Construction of an Amperometric Immunosensor Using Solanum Tuberosum Potato Apyrase for the Detection of Schistosomiasis. Información Tecnológica **20**, 3 (2009). ISSN: 0718–0764
60. K.K. Kasem, S. Jones, Platinum as a reference electrode in electrochemical measurements, Platinum Metal Rev. **52**, 100–106 (Apr 2008)
61. H.E.A. Ferreira, D. Daniel, M. Bertotti, E.M. Richter, A novel disposable electrochemical microcell construction and characterization, J. Brazilian Chem. Soc. **19**, 8 (2008)
62. I. Bontidean, C. Berggren, G. Johansson, E. Csöregi, B. Mattiasson, J.R. Lloyd, K.J. Jakeman, N.L. Brown, Detection of heavy metal ions at femtomolar levels using protein-based biosensors. Anal. Chem. **70**(19), 4162–4169 (1998)
63. E. Katz, I. Willner, Probing biomolecular interactions at conductive and semiconductive surfaces by impedance spectroscopy:Routes to impedimetric immunosensors, DNA-sensors, and enzyme biosensors, Electroanalysis **15**(11), 913–947 (2003)
64. L. Yang, Y. Li, C.L. Griffis, M.G. Johnson, Interdigitated microelectrode (IME) impedance sensor for the detection of ciable Salmonella typhimurium, Biosens. Bioelectron **19**, (10), 1139–1147 (2004)
65. B. Robert, C. Northrop, in *Analysis and Application of Analog Electronic Circuits to Biomedical Instrumentation*, ed. by M.R. Neuman. The Biomedical Engineering Series (CRC Press, Florida, USA, 2004)
66. A. De Marcellis, G. Ferri, M. Patrizi, V. Stornelli, A.D' Amico, C. Di Natale, E. Martinelli, A. Alimelli, R. Paolesse, An integrated analog lock-in amplifier for low-voltage low-frequency sensor interface, in *Proceddings of the Interational Workshop on Advances in Sensors and Interface, IWASI*, pp. 1–5 June 2007
67. D. Rairigh, A. Mason, C. Yang, Analysis of on-chip impedance spectroscopy methodologies for sensor arrays. Sensor. Lett. **4**(4), 398–402 (2006)
68. A.E. Moe, S.R. Marx, I. Bhinderwala, D.M. Wilson, A miniaturuzed lock-in amplifier design suitable for impedance measurements in cells. Proc. IEEE Sens. **1**(24–27), 215–218 (AUTRICHE 2004)
69. W. Xu, E.G. Friedman, Clock Feedthrough in CMOS analog transmission gate switches. Anal. Int. Circuits and Signal Process **44**, 271–281 (2005)
70. R. Hogervost, J.P. Tero, R.G.H. Eschauzier, J.H. Huijsin. A compact power-efficient 3 V CMOS rail-to-rail input/ouput omperational amplifier for VLSI cell libraries. IEEE J. Solid-State Circuits **29**, 1505–1513 (1994)
71. A. Veeravalli, E. Sánchez-Sinencio. J. Silva-Martínez, Transconductance amplifiers with very small transconductances: A comparative design approach. IEEE J. Solid-State Circuits **37**(6), 770–775 (June 2002)
72. A. Arnaud, R. Fiorelli, C. Galup-Montoro, Nanowatt, sub-nS OTAs, with Sub-10-mV input offset, using series-parallel current mirrors. IEEE J. Solid-State Circuits **41**(9), 2009–2018 (Sept 2006)

73. J.M. Fiore, in *Amplificadores Operacionales y Circuitos Integrados Lineales*, ed. by Thomson. (Mohawk Valley Community College, Ed. Paraninfo, Madrid, Spain, 2002)
74. R.S. Machay, *Bio–Medical Telemetry*, 2nd edn. (Wiley, New York, NY, 1970)
75. H.P. Kimmich, in Biotelemetry, eds. by J.G. Webster. *Encyclopedia of Medical Devices and Instrumentation*, (Wiley, New York, NY, 1980)
76. A. Santic, M.R. Neuman, *A low-power infrared biotelemetry system, Biotelemetry VIII*, (Kimmich/Klewe, Netherlands, 1984)
77. S.A.P. Haddad, W.A. Serdijn, Ultra low-power biomedical signal processing: An analog wavelet filter approach for pacemakers, Anal. Circuits and Signal Process. (Springer 2009). ISBN: 978-1-4020-9072-1
78. M.R. Haider, S.K. Islam, M. Zhang, A low-power signal processing unit for in vivo monioring and transmission of sensor signals. Sens. Trans. J. **84**(10), 1625–1632 (2007)
79. Positive ID/Verichip White Paper, Development of an Implantable Glucose Sensor, http://www.positiveidcorp.com/white-papers.html
80. K. Van Schuylengergh, R. Puers, *Inductive Powering. Basic Theory and Application to Biomedical Systems*, (Springer, The Netherlands, 2009). ISBN: 978-90-481-2411-4
81. B. Lenaerts, R. Puers, *Omnidirectional Inductive Powering for Biomedical Implants*, (Springer, The Netherlands, 2009). ISBN: 978-1-4020-9074-5
82. W.C. Lin, S.K. Pillay, A micropower pulsewidht-modulation-pulse-position-modulation two-channel telemetry system for biomedical applications. IEEE Trans. Biomed. Eng. **BME – 21**, 273–280 (1974)
83. C. Weller, Electrocardiography by infrared telemetry. J. Physiol. (London) **267**, 11–12 (1977)
84. Z. Tang, B. Smith, J.H. Schild, P.H. Peckham, Data transmission from an implantable biotelemeter by load-shift keying using circuit configuration modulator. IEEE Trans. Biomed. Eng. **BME-42**, 524–528 (1995)
85. A. Santic, M.R. Neuman, *A low-power infrared biotelemetry system, Biotelemetry VIII*, (Kimmich/Klewe, Netherlands, 1984)
86. H.P. Kimmich, *Biotelemetry, Enciclopedia of Medical Devices and Instrumentation*, (Willey, New York, USA, 1988), pp. 409–425
87. N. Donaldson, Passive signalling via inductive coupling. Med. Biol. Eng. Comput. **24**, 223–224 (1986)
88. D. Gajski, *Principios de Diseño Digital*, (Prentice Hall, Madrid, España, 2000). ISBN: 84-8322-004-0